

Article

# Dry Reforming of Methane over Pyrochlore-Type La<sub>2</sub>Ce<sub>2</sub>O<sub>7</sub>-Supported Ni Catalyst: Effect of Particle Size of Support

 Zeling Zhou <sup>1,2,†</sup>, Chao Li <sup>1,2,†</sup>, Junfeng Zhang <sup>1,\*</sup> , Qiliang Gao <sup>1,2</sup>, Jiahao Wang <sup>1,2</sup>, Qingde Zhang <sup>1</sup> and Yizhuo Han <sup>1,\*</sup>
<sup>1</sup> State Key Laboratory of Coal Conversion, Institute of Coal Chemistry, Chinese Academy of Sciences, Taiyuan 030001, China

<sup>2</sup> University of Chinese Academy of Sciences, Beijing 100049, China

\* Correspondence: zhangjf@sxicc.ac.cn (J.Z.); hanyz@sxicc.ac.cn (Y.H.); Tel.: +86-351-4049747 (Y.H.)

<sup>†</sup> These authors contributed equally to this work.

**Abstract:** The properties of supports (such as oxygen vacancies, oxygen species properties, etc.) significantly impact the anti-carbon ability due to their promotional effect on the activation of CO<sub>2</sub> in dry reforming of methane (DRM). Herein, pyrochlore-type La<sub>2</sub>Ce<sub>2</sub>O<sub>7</sub> compounds prepared using co-precipitation (CP), glycine nitrate combustion (GNC) and sol-gel (S-G) methods, which have highly thermal stability and unique oxygen mobility, are applied as supports to prepare Ni-based catalysts for DRM. The effect of the calcining temperature (500, 600 and 700 °C) on La<sub>2</sub>Ce<sub>2</sub>O<sub>7</sub>(CP) has also been investigated. Based on multi-technique characterizations, it is found that the synthesis method and calcination temperature can influence the particle size of the La<sub>2</sub>Ce<sub>2</sub>O<sub>7</sub> support. Changes in particle size strongly modulate the pore volume, specific surface area and numbers of surface oxygen vacancies of the La<sub>2</sub>Ce<sub>2</sub>O<sub>7</sub> support. As a result, the distribution of supported Ni components is affected due to the different metal-support interaction, thereby altering the activity of the catalysts for cracking CH<sub>4</sub>. Moreover, the supports' abilities to adsorb and activate CO<sub>2</sub> are also adjusted accordingly, accelerating the removal of the carbon deposited on the catalysts. Finally, La<sub>2</sub>Ce<sub>2</sub>O<sub>7</sub>(CP 600) with an appropriate particle size exhibits the best catalytic activity and stability in DRM.

**Keywords:** pyrochlore; nickel; dry reforming; CH<sub>4</sub>; CO<sub>2</sub>



**Citation:** Zhou, Z.; Li, C.; Zhang, J.; Gao, Q.; Wang, J.; Zhang, Q.; Han, Y. Dry Reforming of Methane over Pyrochlore-Type La<sub>2</sub>Ce<sub>2</sub>O<sub>7</sub>-Supported Ni Catalyst: Effect of Particle Size of Support. *Molecules* **2024**, *29*, 1871. <https://doi.org/10.3390/molecules29081871>

Academic Editor: Giorgio Vilardi

Received: 19 March 2024

Revised: 16 April 2024

Accepted: 16 April 2024

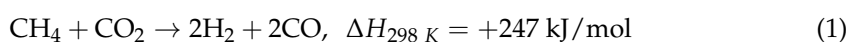
Published: 19 April 2024



**Copyright:** © 2024 by the authors. Licensee MDPI, Basel, Switzerland. This article is an open access article distributed under the terms and conditions of the Creative Commons Attribution (CC BY) license (<https://creativecommons.org/licenses/by/4.0/>).

## 1. Introduction

Methane reforming with carbon dioxide, also known as dry reforming of methane (DRM), which transforms two of the main greenhouse gases (CH<sub>4</sub> and CO<sub>2</sub>) into valuable syngas (as shown in Equation (1)), has increased hopes of efficiently utilizing natural gas and reducing CO<sub>2</sub> emissions [1]. Therefore, the development of Ni-based catalysts for DRM reaction has made significant progress due to their comparable activity to noble metal catalysts.



A prevailing consensus on the catalytic mechanism suggests that Ni-based catalysts play bi-functional roles: CH<sub>4</sub> dissociation and the carbon removal with CO<sub>2</sub>, wherein, CH<sub>4</sub> dissociation takes place on the Ni surface and carbon removal is closely related to the Lewis basic sites, and oxygen species or oxygen vacancies on the catalyst surface [2,3]. Currently, the main issue encountered regarding DRM is that catalyst deactivates gradually with time on stream, primarily attributed to Ni sintering at high temperatures and carbon deposition on the catalyst surface. To mitigate Ni sintering, some measures such as improving Ni

dispersion, preparing the Ni catalyst with embedded or encapsulated configuration were often adopted [4–8], which has been demonstrated to be effective in suppressing Ni particle growth. The occurrence of carbon deposition is due to the unmatched rates between CH<sub>4</sub> dissociation and the carbon removal, with the former exhibiting a relatively higher rate than the latter. Therefore, enhancing the abilities of CO<sub>2</sub> activation and subsequent carbon removal of the employed Ni catalyst is anticipated to further balance the two rates, finally accomplishing commendable catalyst stability.

For a considerable duration, researchers have been devoting their efforts to addressing the challenge of catalyst deactivation caused by carbon deposition as well as low-temperature operation for DRM. As far as research is concerned, the anti-carbon ability of basic sites, generated through the introduction of alkali or alkaline earth metals, has been elaborated in the literature [9], and some important progress has been made. In addition, considering that oxygen species or oxygen vacancies have a positive activation effect on CO<sub>2</sub>, more researchers have paid attention to tuning the properties of oxygen species to investigate the origin of carbon removal. They have demonstrated that the carbonate and formate species on the catalyst surface, formed by CO<sub>2</sub> adsorption and interaction with surficial oxygen vacancies and/or hydroxyl, are able to significantly contribute to the removal of intermediate carbon species. Nagaoka et al. [10] compared the reaction behaviors over Pt/Al<sub>2</sub>O<sub>3</sub> and Pt/ZrO<sub>2</sub> and observed that only a small amount of carbon deposited on the latter catalyst. They deduced that oxygen vacancies originated from ZrO<sub>2</sub> due to its reducibility and then adsorbed and activated CO<sub>2</sub> to form carbonate species, which finally accomplished carbon removal, wherein, following the reaction between carbonate species and intermediate carbon species, the oxygen vacancies were recovered for the next circulation. Similar to ZrO<sub>2</sub>, some other supports possessing oxygen storage capacity, such as CeO<sub>2</sub>, CeZr solid solution, etc., all have obvious promotional effects on CO<sub>2</sub> activation and subsequent carbon removal. Sutthiumporn's [11] and our results [12] demonstrated that the content of lattice oxygen in perovskite catalyst strongly affected CH<sub>4</sub> and CO<sub>2</sub> activation. Budiman et al. [13] found that the reorganization of lattice oxygen caused during catalyst reduction significantly improved the catalyst duration. In our previous study, we regulated the distribution of oxygen species by changing the calcination atmosphere and demonstrated that the surface-adsorbed oxygen species is beneficial for improving DRM performance due to their enhanced abilities of CO<sub>2</sub> activation and carbon removal [14]. Furthermore, we doped transition metals such as Ce, La, Sm and Y into Ni/ZrO<sub>2</sub> and confirmed that the surface-adsorbed oxygen species are certainly effective in promoting CH<sub>4</sub> dissociation and CO<sub>2</sub> activation [15]. As for the carbon removal mechanism, a widely approved viewpoint is that active oxygen species have spillover to the metal surface from the support or metal–support interface and interact with intermediate carbon species and the deposited carbon, finally completing the carbon removal. Yentenkakis et al. [3] investigated the  $\gamma$ -Al<sub>2</sub>O<sub>3</sub>, Al<sub>2</sub>O<sub>3</sub>-Ce<sub>0.5</sub>Zr<sub>0.5</sub>O<sub>2- $\delta$</sub>  and Ce<sub>0.5</sub>Zr<sub>0.5</sub>O<sub>2- $\delta$</sub>  supported Rh catalyst for DRM. They demonstrated that the unstable lattice oxygen could overflow to the surface of Rh, resulting in stabilization of the Rh<sup>0</sup> and oxidization of carbon species; here, the oxygen vacancies over the support produced after oxygen spillover possess the capacity to activate CO<sub>2</sub>. The above convincingly demonstrated that the supports with abundant oxygen species or facile oxygen mobility are very selectable in the context of preparing the catalysts with excellent activity and stability for DRM.

Pyrochlore-type compounds, which have a typical formula of A<sub>2</sub>B<sub>2</sub>O<sub>7</sub>, have highly thermal stability and unique oxygen mobility. Some typical materials such as La<sub>2</sub>Rh<sub>2</sub>O<sub>7</sub> have been applied for DRM reaction in some previous reports. Spivey et al. [16,17] revealed that the existing lattice oxygen in La<sub>2</sub>Rh<sub>2</sub>O<sub>7</sub> support was quite conducive to carbon removal. Zhang et al. [18] reported that the high thermal stability, abundant oxygen vacancies and good oxygen mobility of A<sub>2</sub>B<sub>2</sub>O<sub>7</sub> made Ni/A<sub>2</sub>B<sub>2</sub>O<sub>7</sub> catalyst achieve remarkable performance.

Herein, the present study was focused on the effects of La<sub>2</sub>Ce<sub>2</sub>O<sub>7</sub> supports tuned using different methods, as well as different calcination temperatures, on the catalytic performance of DRM. The origin of variations in La<sub>2</sub>Ce<sub>2</sub>O<sub>7</sub> support properties and the

reaction behavior caused by different preparation methods and different calcination temperatures on reaction behavior over the prepared Ni catalysts was explored in detail. The characterization results revealed that  $\text{La}_2\text{Ce}_2\text{O}_7$  prepared using a co-precipitation method with an appropriate size has more oxygen vacancies, leading to more surface-adsorbed oxygen species and higher content of basic sites for  $\text{CO}_2$  adsorption, which significantly contribute to better activity and stability for DRM.

## 2. Results and Discussion

### 2.1. Structure and DRM Reaction Behaviors over the Catalysts Prepared with Different Methods

#### 2.1.1. Sample Characterization

Figure 1 gives XRD patterns of the prepared  $\text{La}_2\text{Ce}_2\text{O}_7$  supports and Ni-loaded and reduced catalysts. As seen in Figure 1a, all the prepared supports show characteristic diffraction peaks ascribed to pyrochlore crystalline (JCPDS#04-12-6396), without observable diffraction peaks associated with  $\text{La}_2\text{O}_3$  and  $\text{CeO}_2$ , wherein the enhanced diffraction peaks for  $\text{La}_2\text{Ce}_2\text{O}_7$ (S-G) reveal that the sol–gel method is seemingly more favorable for high crystallization. This indicates that the aforementioned three preparation methods are available to prepare the pure pyrochlore crystalline. As shown in Figure 1b, the introduction of NiO has a limited effect on the pyrochlore structure, and characteristic diffraction peaks of NiO at  $37.3^\circ$ ,  $43.3^\circ$ ,  $62.9^\circ$  and  $75.4^\circ$  are not observable [19], indicating that the introduced NiO is highly dispersed on supports. Turning the focus to the XRD patterns of the reduced catalysts (Figure 1c), it is found that when the catalysts suffered from the reduction treatment at  $700^\circ\text{C}$ , the crystalline levels of  $\text{La}_2\text{Ce}_2\text{O}_7$ (GNC) and  $\text{La}_2\text{Ce}_2\text{O}_7$ (CP 500) are enhanced while that of  $\text{La}_2\text{Ce}_2\text{O}_7$ (S-G) has not changed, whereas there are still no diffraction peaks ascribed to metal Ni observed. Based on the XRD results, the crystalline size of the representative samples was calculated using the Scherrer equation. As listed in the right-hand column of Table 1,  $\text{La}_2\text{Ce}_2\text{O}_7$ (CP 500) shows the smallest particle size (56 nm),  $\text{La}_2\text{Ce}_2\text{O}_7$ (GNC) is comparable to  $\text{La}_2\text{Ce}_2\text{O}_7$ (CP 500), and, nevertheless,  $\text{La}_2\text{Ce}_2\text{O}_7$ (S-G) possesses a particle size as large as 229 nm. As for the reduced catalysts, the particle size of Ni/ $\text{La}_2\text{Ce}_2\text{O}_7$ (CP 500) and Ni/ $\text{La}_2\text{Ce}_2\text{O}_7$ (GNC) shows an obvious increase, which is attributed to the improvement of the crystalline level. This phenomenon may be because the calcination temperature is  $500^\circ\text{C}$ , while the reduction temperature is  $700^\circ\text{C}$ . The small particle  $\text{La}_2\text{Ce}_2\text{O}_7$  supports have undergone further sintering during the higher temperature reduction process, while the large particle support was more difficult to sinter.

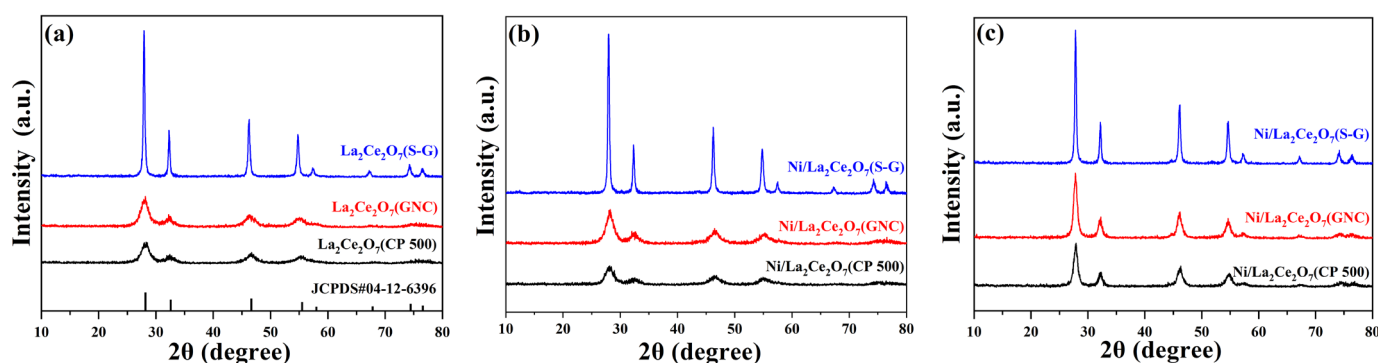


**Figure 1.** XRD patterns of the prepared  $\text{La}_2\text{Ce}_2\text{O}_7$  supports (a), Ni-loaded (b) and reduced catalysts (c).

Figure 2a–d show the  $\text{N}_2$  adsorption–desorption isotherms and pore size distribution of the prepared supports and Ni-loaded catalysts. From Figure 2a, it can be observed that all prepared supports show IV-type isotherms, indicating their mesoporous characteristics, whereas the relatively small H2-type hysteresis loop of  $\text{La}_2\text{Ce}_2\text{O}_7$ (S-G) implies that it has a poor mesoporous structure. This phenomenon suggests that the variations in support particle size will affect the pore structure. The pore size distribution in Figure 2b further illustrates that the pore widths of  $\text{La}_2\text{Ce}_2\text{O}_7$ (GNC) and  $\text{La}_2\text{Ce}_2\text{O}_7$ (CP 500) are predomi-

nantly centralized within the range of 5–40 nm. In the case of Ni-loaded catalysts, it is plausible that Ni introduction rarely affects the pore mesoporous structure; nevertheless, the pore distribution is further shrunk within 5–30 nm.

**Table 1.** The physical properties of the  $\text{La}_2\text{Ce}_2\text{O}_7$  supports and supported catalysts.

Sample	Specific Surface Area ( $\text{m}^2/\text{g}$ )	Pore Volume ( $\text{cm}^3/\text{g}$ )	Average Pore Diameter (nm)	Crystalline Size <sup>a</sup> (nm)
$\text{La}_2\text{Ce}_2\text{O}_7(\text{CP 500})$	35.2	0.1105	12.6	56
$\text{La}_2\text{Ce}_2\text{O}_7(\text{GNC})$	20.5	0.0575	11.2	60
$\text{La}_2\text{Ce}_2\text{O}_7(\text{S-G})$	12.9	0.0398	12.3	229
$\text{Ni}/\text{La}_2\text{Ce}_2\text{O}_7(\text{CP 500})$	33.5	0.1127	13.4	95 *
$\text{Ni}/\text{La}_2\text{Ce}_2\text{O}_7(\text{GNC})$	16.7	0.0613	14.7	108 *
$\text{Ni}/\text{La}_2\text{Ce}_2\text{O}_7(\text{S-G})$	13.8	0.0549	15.9	224 *

<sup>a</sup> Calculated using the Scherrer equation according to the (111) crystal surface reflection of XRD results. \* The crystalline size of the reduced catalysts.

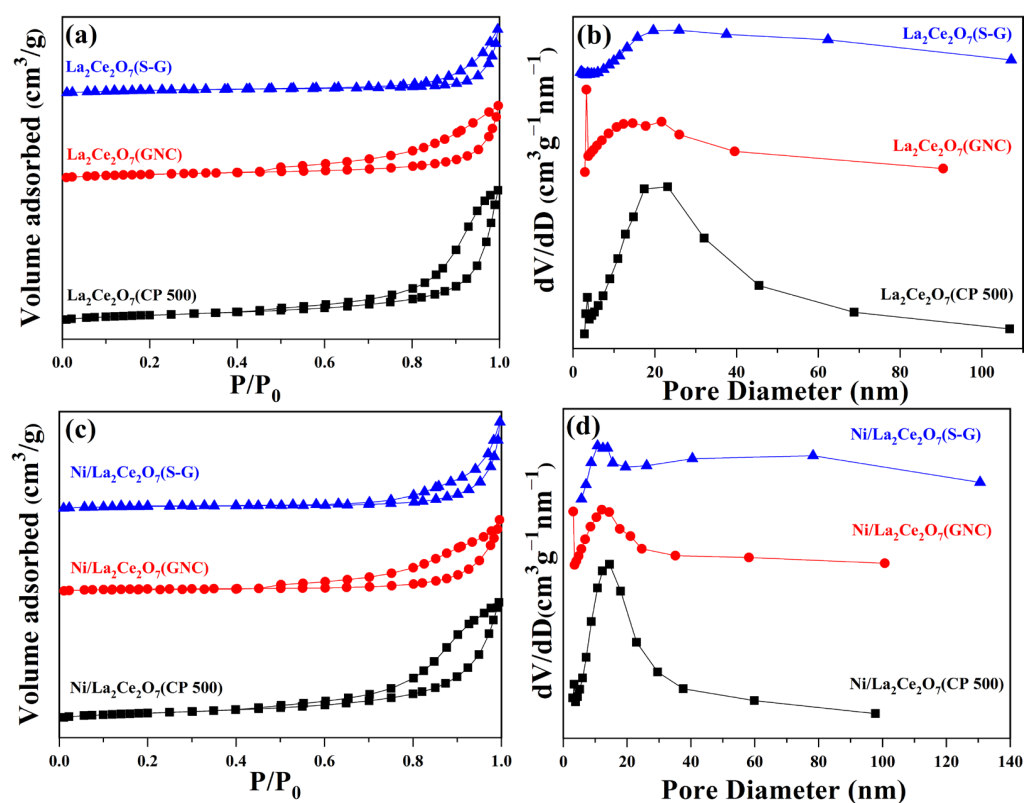


**Figure 2.**  $\text{N}_2$  isotherms and pore distribution of the prepared supports (a,b) and Ni-loaded catalysts (c,d).

Based on the  $\text{N}_2$  sorption data, the textural parameter of the  $\text{La}_2\text{Ce}_2\text{O}_7$  supports and supported catalysts were calculated, and the results are shown in Table 1. For the prepared support, the  $\text{La}_2\text{Ce}_2\text{O}_7(\text{CP 500})$  shows the largest BET surface area ( $35.2 \text{ m}^2/\text{g}$ ), followed by  $\text{La}_2\text{Ce}_2\text{O}_7(\text{GNC})$ .  $\text{La}_2\text{Ce}_2\text{O}_7(\text{S-G})$  shows the smallest BET surface area, probably attributed to its larger particle size and inadequate porous structure. The trend in change in the pore volume is consistent with BET surface, suggesting the contribution effect of the mesoporous structure. For the supported catalysts,  $\text{Ni}/\text{La}_2\text{Ce}_2\text{O}_7(\text{CP 500})$  and  $\text{Ni}/\text{La}_2\text{Ce}_2\text{O}_7(\text{GNC})$  show a decrease in specific surface area and little change in pore volume compared to their corresponding supports, while the specific surface area and pore volume have a certain growth when  $\text{La}_2\text{Ce}_2\text{O}_7(\text{S-G})$  is loaded with Ni. This indicates that the particle size of the supports affects the dispersion of the loaded Ni. Additionally, the average pore size of the catalysts after loading Ni has been improved compared to the corresponding supports,

which may be due to the formation of stacked pores on the surface of Ni particles, resulting in changes in the pore distribution of the catalysts.

Catalyst activity and stability are not only related to the physical properties (such as particle size, pore structure) but also affected by the interaction between active component and support [20]. The reducibility of the catalysts was characterized using the H<sub>2</sub>-TPR technique, and the results are shown in Figure 3a. As observed, the Ni/La<sub>2</sub>Ce<sub>2</sub>O<sub>7</sub>(CP 500) exhibits a major H<sub>2</sub> consumption peak at 351 °C, accompanied by a satellite peak at 236 °C. Referring to the reduction peak of pure NiO, it is deduced that the small peak at low temperature is associated with the reduction of NiO particles dispersed on the support surface, which exist in an isolated state and weakly interact with the support [21], while the peak at high temperature is attributed to the reduction of the NiO interacting with the support. In theory, strong metal–support interaction is beneficial for improving Ni dispersion and enhancing the anti-sintering performance of the catalyst. The reduction peak at 351 °C on Ni/La<sub>2</sub>Ce<sub>2</sub>O<sub>7</sub>(GNC) is quite similar to that on Ni/La<sub>2</sub>Ce<sub>2</sub>O<sub>7</sub>(CP 500), whereas the peak area on the former is obviously smaller than that on the latter. This indicates that there are more reducible Ni species over the Ni/La<sub>2</sub>Ce<sub>2</sub>O<sub>7</sub>(CP 500). The lowest reduction temperature (336 °C) of Ni/La<sub>2</sub>Ce<sub>2</sub>O<sub>7</sub>(S-G) suggests the weakest interaction between NiO and the La<sub>2</sub>Ce<sub>2</sub>O<sub>7</sub>(S-G) support. We deduce that the particle size of supports affects the state of oxygen species on the catalyst surface and porous properties, consequently impacting the existence state of Ni species, thereby resulting in distinct reduction behaviors over the three catalysts.

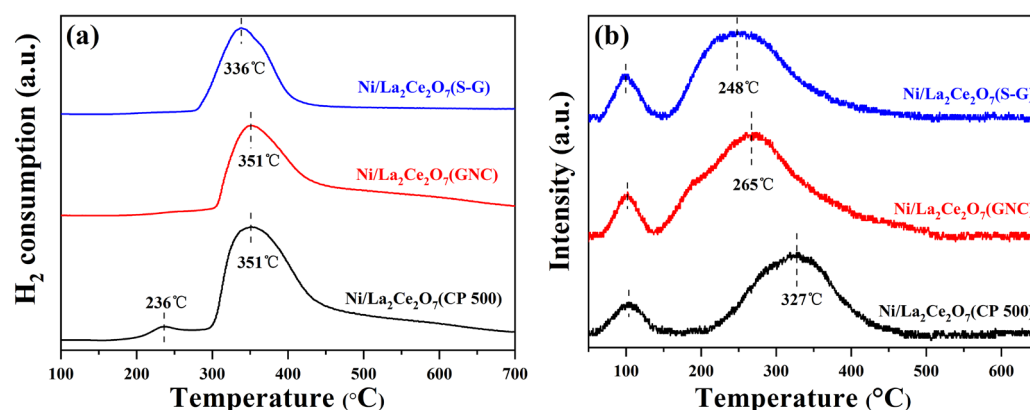
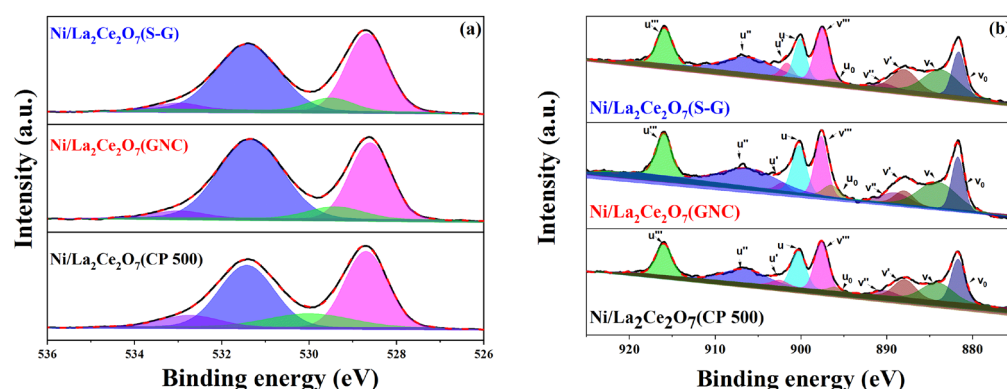


Figure 3. H<sub>2</sub>-TPR (a) and CO<sub>2</sub>-TPD (b) profiles of Ni/La<sub>2</sub>Ce<sub>2</sub>O<sub>7</sub> catalysts.

The basicity properties of the catalyst prepared with different methods were investigated using the CO<sub>2</sub>-TPD technique. For each operation, the sample was first pre-reduced at 700 °C. Figure 3b presents the CO<sub>2</sub>-TPD curves. As observed, the three catalysts all exhibit two CO<sub>2</sub> desorption peaks, wherein the one at 100 °C is ascribed to the weak basic sites on the catalyst surface, which could be assigned to the reactive bicarbonates originated from weak interactions between hydroxyl groups on pyrochlore surface and CO<sub>2</sub> [22], and the other one is related to strong adsorption of CO<sub>2</sub>. Compared to the desorption at high temperature, it is apparent that Ni/La<sub>2</sub>Ce<sub>2</sub>O<sub>7</sub>(CP 500) possesses the strongest basicity within three catalysts, and Ni/La<sub>2</sub>Ce<sub>2</sub>O<sub>7</sub>(S-G) has the weakest basicity. For DRM reaction, the ability of CO<sub>2</sub> adsorption strongly affects the catalytic performance. Specifically, the robust adsorption of CO<sub>2</sub> is able to furnish relatively many oxygen species to remove inert carbon species at the transition state, and it can alleviate the accumulation of the carbon deposit, thus prolonging the catalyst's lifetime [23]. Based on the above, the strong basicity on Ni/La<sub>2</sub>Ce<sub>2</sub>O<sub>7</sub>(CP 500) is expected to exert a positive effect on DRM running over a long period.

To understand the existing state of the component in a catalyst, the reduced catalysts were characterized using the XPS technique. Figure 4a shows XPS spectra of O1s and the corresponding fitted results, where the peak at 528.6 eV is ascribed to surface lattice oxygen

species [14] and the one at 531.5 eV is associated with carbonate species [24]. Moreover, another two peaks at 533 and 529.5 eV are also observed, which are thought to be related to superoxide ions ( $O_2^-$ ) and peroxy ions ( $O_2^{2-}$ ), respectively [25]. Some research has indicated that electrophilic oxygen species ( $O_2^-$ ,  $O_2^{2-}$ ) are closely related to the oxygen vacancy on the surface [26]. Here, the percentage of oxygen vacancy can be presented as  $(O_2^- + O_2^{2-})/O^{2-}$  [27,28]. Another study also indicated that oxygen vacancies are able to play remarkably positive roles in absorbing and activating  $CO_2$  [29,30], which is effective to suppressing carbon deposition. The percentage of different oxygen species on the surface is normalized and listed in Table 2. As observed, the value of  $(O_2^- + O_2^{2-})/O^{2-}$  declines in the following order: Ni/La<sub>2</sub>Ce<sub>2</sub>O<sub>7</sub>(CP 500) > Ni/La<sub>2</sub>Ce<sub>2</sub>O<sub>7</sub>(GNC) > Ni/La<sub>2</sub>Ce<sub>2</sub>O<sub>7</sub>(S-G). This suggests that the most oxygen vacancies are presented on Ni/La<sub>2</sub>Ce<sub>2</sub>O<sub>7</sub>(CP 500), thereby facilitating the adsorption and activation of  $CO_2$ .



**Figure 4.** (a) XPS profiles of reduced Ni/La<sub>2</sub>Ce<sub>2</sub>O<sub>7</sub> catalysts (O1s); (b) XPS analysis of Ce<sup>3+</sup>/Ce<sup>4+</sup> on the surface of Ni/La<sub>2</sub>Ce<sub>2</sub>O<sub>7</sub> catalysts.

**Table 2.** The XPS quantification results of the Ni/La<sub>2</sub>Ce<sub>2</sub>O<sub>7</sub> catalysts.

Catalyst	Ce <sup>3+</sup> (%)	Ni Atomic Concentration (%)	O 1s B.E (eV)/Relative Amount (%)				$(\alpha + \beta)/\gamma$
			O <sub>2</sub> <sup>-</sup> ( $\alpha$ )	CO <sub>3</sub> <sup>2-</sup>	O <sub>2</sub> <sup>2-</sup> ( $\beta$ )	O <sup>2-</sup> ( $\gamma$ )	
Ni/La <sub>2</sub> Ce <sub>2</sub> O <sub>7</sub> (S-G)	21	4.06	533.0/2.9	531.4/50.3	529.5/7.0	528.7/39.8	0.25
Ni/La <sub>2</sub> Ce <sub>2</sub> O <sub>7</sub> (GNC)	25	4.66	533.0/3.6	531.3/55.1	529.4/7.2	528.6/34.1	0.32
Ni/La <sub>2</sub> Ce <sub>2</sub> O <sub>7</sub> (CP 500)	27	4.69	533.0/7.8	531.4/40.2	530.0/13.4	528.7/38.6	0.54

For the catalysts containing a Ce component, as reported in the literature, the amount of electrophilic oxygen species is related to the concentration of Ce<sup>3+</sup> on the surface [31,32]. Figure 4b presents the Ce2p XPS spectra of the reduced catalysts, wherein the fitted peaks for v<sub>0</sub>, v', u<sub>0</sub> and u' are related to Ce<sup>3+</sup> species, while the peaks for v, v'', v''', u, u'' and u''' are associated with Ce<sup>4+</sup> species. The discernible binding energies assigned to Ce<sup>3+</sup> and Ce<sup>4+</sup> species are evidently observed, due to the facile transformation from Ce<sup>3+</sup> and Ce<sup>4+</sup>. Based on the obtained fitted result, we subsequently determined the percentage of Ce<sup>3+</sup> using the following equation [31,32], and the corresponding results are tabulated in Table 2. It is observed that the Ce<sup>3+</sup> percentage is arranged in the following order: Ni/La<sub>2</sub>Ce<sub>2</sub>O<sub>7</sub>(CP 500) > La<sub>2</sub>Ce<sub>2</sub>O<sub>7</sub>(GNC) > La<sub>2</sub>Ce<sub>2</sub>O<sub>7</sub>(S-G), which is consistent with the sequence of the amount of oxygen species. This indicates that oxygen species on the catalyst surface are closely related to the valence of Ce species.

$$Ce^{3+}(\%) = \frac{Ce^{3+}}{Ce^{3+} + Ce^{4+}} \times 100\% \quad (2)$$

Based on the XPS results, the Ni elemental concentration was obtained. As seen in Table 2, the most Ni content is presented on Ni/La<sub>2</sub>Ce<sub>2</sub>O<sub>7</sub>(CP 500), adjacent to that on

Ni/La<sub>2</sub>Ce<sub>2</sub>O<sub>7</sub>(GNC), whereas Ni/La<sub>2</sub>Ce<sub>2</sub>O<sub>7</sub>(S-G) shows the minimum Ni content, probably attributed to the immersion of partial Ni into the bulk.

The morphology of the catalysts was observed via TEM characterization, as shown in Figure 5. For Ni/La<sub>2</sub>Ce<sub>2</sub>O<sub>7</sub>(CP 500) (Figure 5a), Ni nanoparticles are evenly distributed on the La<sub>2</sub>Ce<sub>2</sub>O<sub>7</sub>(CP 500) support, and the average size of particles is centered at 14.6 nm. In the case of Ni/La<sub>2</sub>Ce<sub>2</sub>O<sub>7</sub>(GNC) and Ni/La<sub>2</sub>Ce<sub>2</sub>O<sub>7</sub>(S-G), obvious growth of Ni particles occurred and particle sizes of Ni on them increased to 16.1 and 16.8 nm, respectively, which is attributed to their relatively large particle size for supports and small BET area. From the particle distribution plot in Figure 5c, it is further worth noting that Ni particle is not well dispersed on Ni/La<sub>2</sub>Ce<sub>2</sub>O<sub>7</sub>(GNC).

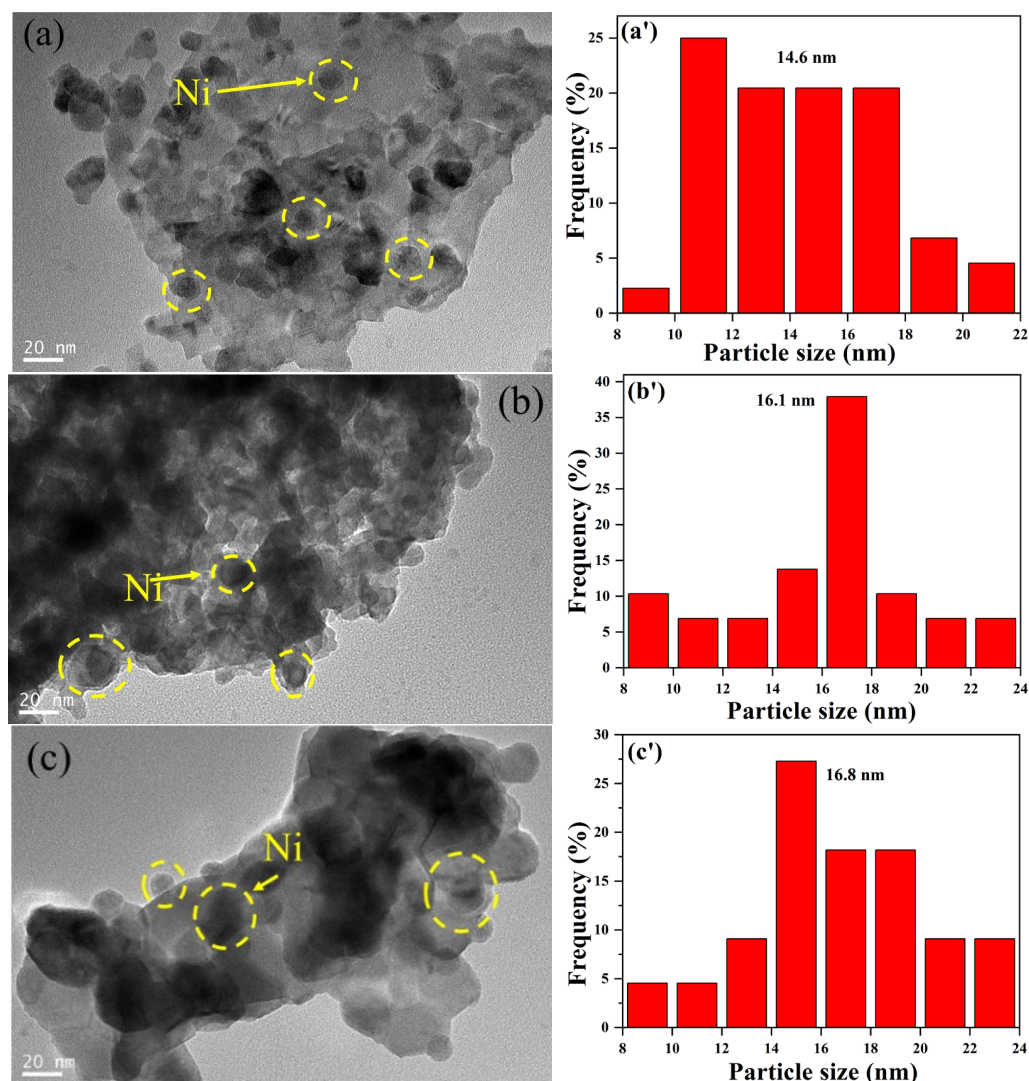


**Figure 5.** TEM images of the reduced catalysts: (a) Ni/La<sub>2</sub>Ce<sub>2</sub>O<sub>7</sub>(CP 500), (b) Ni/La<sub>2</sub>Ce<sub>2</sub>O<sub>7</sub>(GNC), (c) Ni/La<sub>2</sub>Ce<sub>2</sub>O<sub>7</sub>(S-G); particle size distribution of the reduced catalysts: (a') Ni/La<sub>2</sub>Ce<sub>2</sub>O<sub>7</sub>(CP 500), (b') Ni/La<sub>2</sub>Ce<sub>2</sub>O<sub>7</sub>(GNC), (c') Ni/La<sub>2</sub>Ce<sub>2</sub>O<sub>7</sub>(S-G).

Based on the above, it is concluded that La<sub>2</sub>Ce<sub>2</sub>O<sub>7</sub> supports prepared using different preparation methods have different particle sizes, in the order of Ni/La<sub>2</sub>Ce<sub>2</sub>O<sub>7</sub>(S-G) > Ni/La<sub>2</sub>Ce<sub>2</sub>O<sub>7</sub>(GNC) > Ni/La<sub>2</sub>Ce<sub>2</sub>O<sub>7</sub>(CP 500). The smaller the size of the support particles, the larger the BET surface area, the more developed the pore structure, the stronger the metal-support interaction, and the richer the surface O vacancies are. Moreover, supports below 100 nm increase in particle size after loading Ni and reducing at 700 °C.

### 2.1.2. DRM Performance of the Ni/La<sub>2</sub>Ce<sub>2</sub>O<sub>7</sub> Catalyst

Figure 6 gives the conversions of CH<sub>4</sub> and CO<sub>2</sub> and the ratio of H<sub>2</sub>/CO as a function of time on stream. The CH<sub>4</sub> and CO<sub>2</sub> conversions decrease inordinately on the three catalysts with the increase in reaction time. In the evaluation period, Ni/La<sub>2</sub>Ce<sub>2</sub>O<sub>7</sub>(CP 500) shows the optimal catalytic performance, followed by Ni/La<sub>2</sub>Ce<sub>2</sub>O<sub>7</sub>(GNC) and Ni/La<sub>2</sub>Ce<sub>2</sub>O<sub>7</sub>(S-G). Further comparing the deactivation rate, the activity of Ni/La<sub>2</sub>Ce<sub>2</sub>O<sub>7</sub>(CP 500) is seemingly somewhat alleviated, suggesting that it is more durable than the other two. The above characterizations revealed that different preparation methods caused different support particle sizes, which strongly affected the catalyst performance. Since the La<sub>2</sub>Ce<sub>2</sub>O<sub>7</sub>(CP 500) support possesses a relatively larger BET area and a well-developed pore structure, the formed highly dispersed Ni particles on the support surface certainly favor for CH<sub>4</sub> dissociation. Simultaneously, the more oxygen vacancies and strong basic sites over Ni/La<sub>2</sub>Ce<sub>2</sub>O<sub>7</sub>(CP 500) are conducive to the adsorption and activation of CO<sub>2</sub>, further promoting the removal of carbon. In Figure 6b, higher CO<sub>2</sub> conversion on Ni/La<sub>2</sub>Ce<sub>2</sub>O<sub>7</sub>(CP 500) compared to the other two catalysts reflects its more superior promotional impact on CO<sub>2</sub> reactivity. For the Ni/La<sub>2</sub>Ce<sub>2</sub>O<sub>7</sub>(S-G), as indicated by the above characterizations, the relatively large particle size for support results in inadequate porous structure and BET area. Consequently, there is insufficient dispersion of the introduced Ni components, together with weak interaction with active Ni and support and basic sites and low content of oxygen vacancies; as a result, the catalytic performance is the poorest. As shown in Figure 6c, the ratio of H<sub>2</sub>/CO is below 1 due to the RWGS reaction ( $\text{H}_2 + \text{CO}_2 \rightarrow \text{H}_2\text{O} + \text{CO}$ ) and decreases with time on stream [22], wherein the ratio value of H<sub>2</sub>/CO represents the level of RWGS. Seemingly, a more severe RWGS reaction proceeds on Ni/La<sub>2</sub>Ce<sub>2</sub>O<sub>7</sub>(S-G) than the other two.

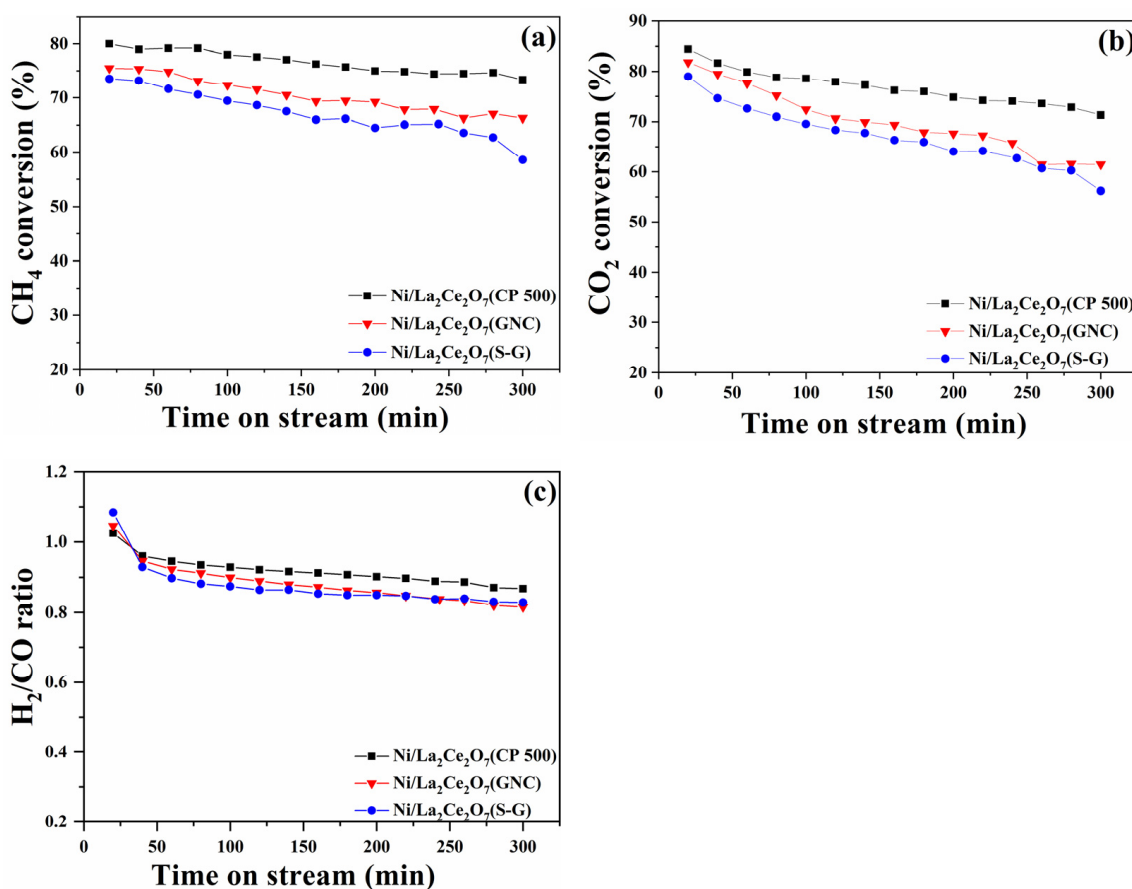


**Figure 6.** Dependence of performance of the prepared Ni/La<sub>2</sub>Ce<sub>2</sub>O<sub>7</sub> on reaction time: (a) CH<sub>4</sub> conversion, (b) CO<sub>2</sub> conversion, (c) H<sub>2</sub>/CO ratio. (reaction conditions: 700 °C, GHSV = 48,000 mL/(g·h) with CH<sub>4</sub>/CO<sub>2</sub> = 1/1).

### 2.1.3. Characterization of the Spent Catalyst

In order to investigate the cause of  $\text{La}_2\text{Ce}_2\text{O}_7$ -supported catalyst deactivation, the spent catalysts were characterized. Figure 7a shows the XRD spectra of  $\text{Ni}/\text{La}_2\text{Ce}_2\text{O}_7$  catalysts after the reaction. As seen, the spent  $\text{Ni}/\text{La}_2\text{Ce}_2\text{O}_7$  catalysts exhibit similar diffraction peaks to the fresh ones, indicating that the original crystalline shape is well kept. For the spent  $\text{Ni}/\text{La}_2\text{Ce}_2\text{O}_7(\text{S-G})$  and  $\text{Ni}/\text{La}_2\text{Ce}_2\text{O}_7(\text{GNC})$  catalysts, the diffraction peaks of graphitic carbon appear at  $26.3^\circ$ , denoting that there is a more obvious occurrence of carbon accumulation on these two catalysts, whereas there is no diffraction peak attributed to graphitic carbon over the  $\text{Ni}/\text{La}_2\text{Ce}_2\text{O}_7(\text{CP 500})$  catalyst, demonstrating its good carbon deposition resistance. Figure 7b shows the thermo-gravimetric curve of the spent catalysts. It is evident that the  $\text{Ni}/\text{La}_2\text{Ce}_2\text{O}_7(\text{CP 500})$  catalyst exhibits a weight loss of only 13.17%, showing a high resistance to carbon accumulation. In contrast, the  $\text{Ni}/\text{La}_2\text{Ce}_2\text{O}_7(\text{S-G})$  and  $\text{Ni}/\text{La}_2\text{Ce}_2\text{O}_7(\text{GNC})$  catalysts manifest higher carbon accumulation, reaching approximately 45%. This also corresponds to the above XRD results.

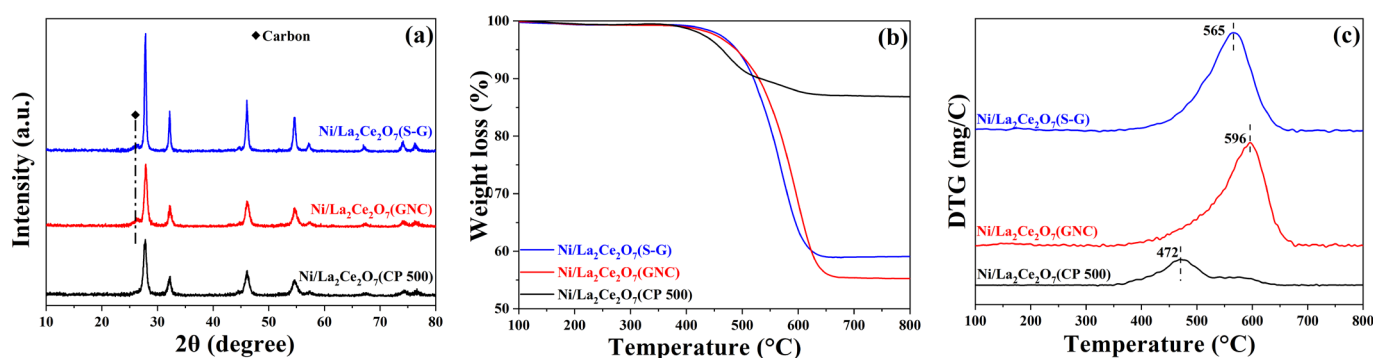


**Figure 7.** XRD profiles (a), TG profiles (b) and DTA profiles (c) of the spent  $\text{Ni}/\text{La}_2\text{Ce}_2\text{O}_7$  catalysts.

The activity of the catalyst surface-deposited carbon was determined from the peaks in the DTA curves. As shown in Figure 7c, the peaks of the DTA curves for the three catalysts appear during two different temperature intervals. According to the literature [33,34], three types of carbon are formed after  $\text{CH}_4$  cracking:  $\text{C}_\alpha$ ,  $\text{C}_\beta$  and  $\text{C}_\gamma$ , and the order of oxidation activity is as follows:  $\text{C}_\alpha > \text{C}_\beta > \text{C}_\gamma$ . Specifically, the  $\text{Ni}/\text{La}_2\text{Ce}_2\text{O}_7(\text{CP 500})$  catalyst has a lower exothermic peak at  $472^\circ\text{C}$  attributed to the more active  $\text{C}_\beta$ , which can react with  $\text{CO}_2$  to form  $\text{CO}$ . However, it should be kept in mind that the formed  $\text{C}_\beta$  encapsulates the active  $\text{Ni}$  component, thereby causing catalyst deactivation. In the case of the  $\text{Ni}/\text{La}_2\text{Ce}_2\text{O}_7(\text{S-G})$  and  $\text{Ni}/\text{La}_2\text{Ce}_2\text{O}_7(\text{GNC})$  catalysts, exothermic peaks classified as  $\text{C}_\gamma$  in the high-temperature region were observed, which is graphitic carbon [35]. Owing to its high inertness, graphitic carbon has relatively low reactivity and is difficult to gasify with  $\text{CO}_2$  under reaction conditions. With a prolonged reaction time, graphite carbon is further formed and wrapped around the active  $\text{Ni}$  particles, which prevents reactant molecules from accessing the active center, ultimately accelerating the deactivation of the catalyst [36,37].

As illustrated in Figure 6, the  $\text{Ni}/\text{La}_2\text{Ce}_2\text{O}_7(\text{S-G})$  and  $\text{Ni}/\text{La}_2\text{Ce}_2\text{O}_7(\text{GNC})$  catalysts deactivate faster. It is widely recognized that the key factors leading to the deactivation of  $\text{Ni}$ -based catalysts are the sintering of  $\text{Ni}$  and carbon deposition. No obvious diffraction peaks of  $\text{Ni}$  are observed from the XRD spectra of the spent catalysts. This indicates that the sintering of  $\text{Ni}$  on this catalyst was not serious. Thus, it is plausible that carbon deposition is the main reason for the faster deactivation.

### 2.2. DRM Reaction Behaviors over $\text{Ni}/\text{La}_2\text{Ce}_2\text{O}_7(\text{CP T})$ Catalysts Obtained through Calcination at Different Temperatures

Through the aforementioned investigation, we have realized that the  $\text{Ni}/\text{La}_2\text{Ce}_2\text{O}_7(\text{CP 500})$  catalyst exhibits the best catalytic performance in DRM due to a relatively smaller support particle size. Furthermore, pre-reduction in  $700^\circ\text{C}$  may induce the aggregation of

the small particles of the support. The impact of the calcination temperature on the support particle size and reactivity of the corresponding Ni-based catalyst in the DRM reaction remains unclear. Herein, in this section, the Ni/La<sub>2</sub>Ce<sub>2</sub>O<sub>7</sub>(CP, T) with different calcination temperatures (500, 600, and 700 °C) was utilized to further investigate the effect of support particle size on the performance in the DRM reaction.

### 2.2.1. Sample Characterization

Figure 8 displays the XRD patterns of the supports calcined at different temperatures and the Ni-loaded and reduced catalysts. From Figure 8a, the intensity of the diffraction peaks is enhanced with the elevation of the calcination temperature, suggesting that the calcination temperature led to the increase in crystal size of the supports, as also indicated in Table 3. For the supported catalysts (Figure 8b), the absence of diffraction peaks attributed to NiO indicates that NiO has been highly dispersed on the supports. Surprisingly, three catalysts suffering from H<sub>2</sub> pre-reduction show a comparable intensity in terms of the diffraction peak. It is deduced that the support was aggregated into larger crystals due to pre-reduction at 700 °C. No diffraction peaks of metal Ni suggests that the reduction treatment does not affect the Ni dispersion. The above results imply that the higher the temperature is, the larger the support particle size is, regardless of the calcination or reduction process.

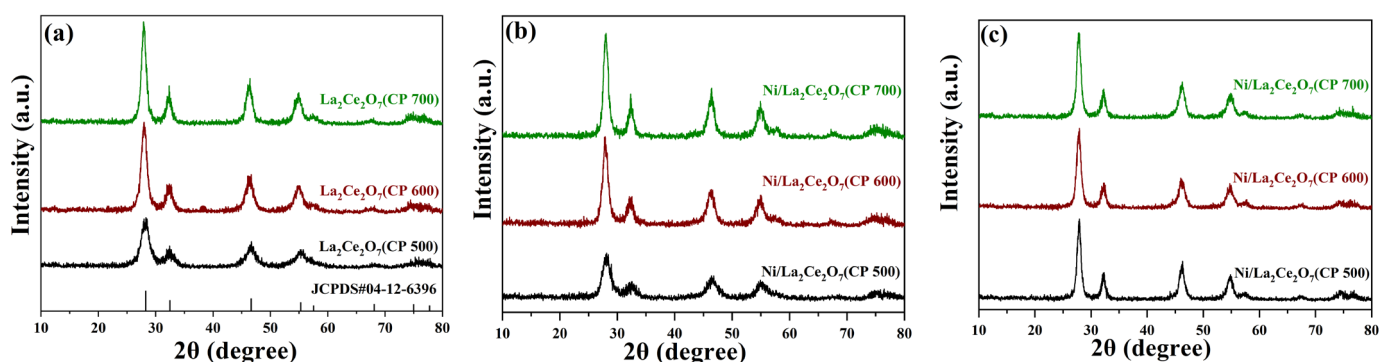


**Figure 8.** XRD patterns of the prepared La<sub>2</sub>Ce<sub>2</sub>O<sub>7</sub> (CP T) supports (a), Ni-loaded (b) and reduced (c) catalysts.

**Table 3.** The physical properties of the La<sub>2</sub>Ce<sub>2</sub>O<sub>7</sub> supports and supported catalysts.

Sample	Specific Surface Area (m <sup>2</sup> /g)	Pore Volume (cm <sup>3</sup> /g)	Average Pore Diameter (nm)	Crystalline Size <sup>a</sup> (nm)
La <sub>2</sub> Ce <sub>2</sub> O <sub>7</sub> (CP 500)	35.21	0.1105	12.55	56
La <sub>2</sub> Ce <sub>2</sub> O <sub>7</sub> (CP 600)	27.91	0.1142	16.36	68
La <sub>2</sub> Ce <sub>2</sub> O <sub>7</sub> (CP 700)	26.21	0.1065	16.26	88
Ni/La <sub>2</sub> Ce <sub>2</sub> O <sub>7</sub> (CP 500)	33.53	0.1127	13.44	95 *
Ni/La <sub>2</sub> Ce <sub>2</sub> O <sub>7</sub> (CP 600)	28.00	0.1156	16.51	87 *
Ni/La <sub>2</sub> Ce <sub>2</sub> O <sub>7</sub> (CP 700)	28.24	0.1205	17.06	91 *

<sup>a</sup> Calculated using the Scherrer equation according to the (111) crystal surface reflection of XRD results. \* The crystalline size of the reduced catalysts.

The samples are further characterized through N<sub>2</sub> sorption at low temperature. The isotherms reveal that all samples maintained a good mesoporous structure, whereas Ni introduction slightly narrows the pore diameter distribution (Figure S1). As seen in Table 3, the BET surface area decreases with the increase in calcination temperature. The changes in BET surface area after loading Ni on the three supports are not consistent. These differences indicate that dispersion of Ni is affected by the particle size of the support. Although the pore volumes of all three supports increase after loading Ni, the changes in La<sub>2</sub>Ce<sub>2</sub>O<sub>7</sub>(CP 500) and La<sub>2</sub>Ce<sub>2</sub>O<sub>7</sub>(CP 600) are almost negligible, while the changes in La<sub>2</sub>Ce<sub>2</sub>O<sub>7</sub>(CP 700) are significant. Differences in pore volume changes before and after

loading Ni on three pyrochlore supports also demonstrate the influence of the support particle size on the Ni distribution.

H<sub>2</sub>-TPR results of the Ni/La<sub>2</sub>Ce<sub>2</sub>O<sub>7</sub>(CP T) catalysts are shown in Figure 9a. As observed, the Ni/La<sub>2</sub>Ce<sub>2</sub>O<sub>7</sub>(CP 500) catalyst has a higher peak hydrogen consumption temperature, followed by Ni/La<sub>2</sub>Ce<sub>2</sub>O<sub>7</sub>(CP 600), and Ni/La<sub>2</sub>Ce<sub>2</sub>O<sub>7</sub>(CP 700) has the lowest reduction temperature. However, the temperatures of the H<sub>2</sub> consumption peaks of Ni/La<sub>2</sub>Ce<sub>2</sub>O<sub>7</sub>(CP 500) and Ni/La<sub>2</sub>Ce<sub>2</sub>O<sub>7</sub>(CP 600) catalysts are very close to each other, indicating that the interactions between the active component and the support on both catalysts were very close. The shift in the H<sub>2</sub> consumption peak of the Ni/La<sub>2</sub>Ce<sub>2</sub>O<sub>7</sub>(CP 700) to a lower temperature suggests that the interaction is weak on this catalyst, ascribed to the fact that larger support particles may lead to weaker metal–support interactions.

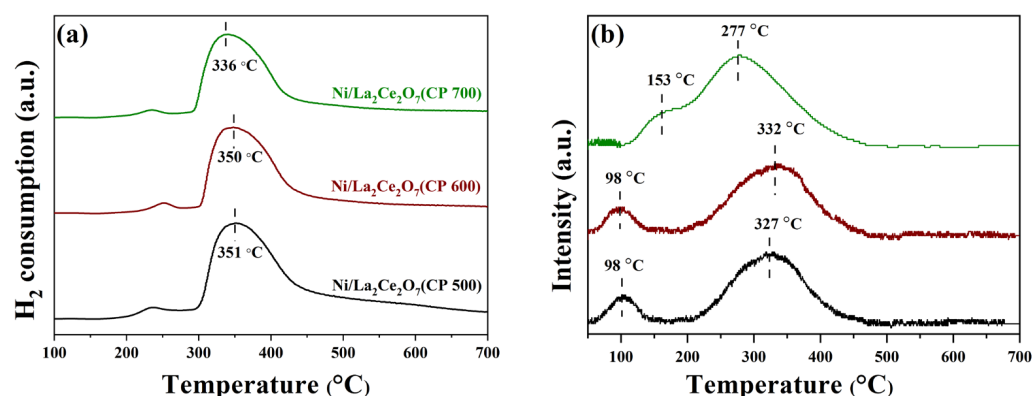
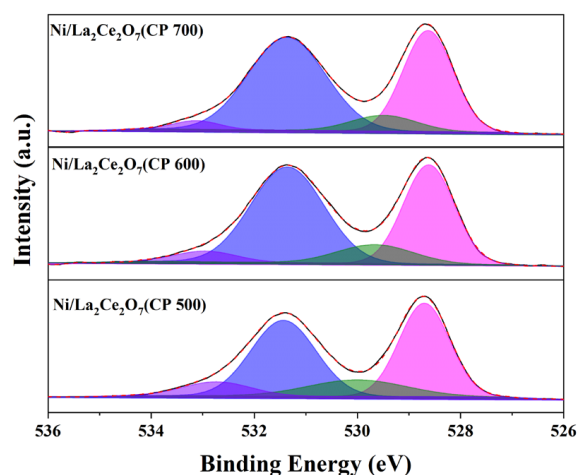


Figure 9. H<sub>2</sub>-TPR (a) and CO<sub>2</sub>-TPD (b) profiles of the Ni/La<sub>2</sub>Ce<sub>2</sub>O<sub>7</sub> (CP T) catalysts.

Figure 9b shows the CO<sub>2</sub>-TPD results of the Ni-loaded La<sub>2</sub>Ce<sub>2</sub>O<sub>7</sub>(CP T) samples. Three catalysts have two CO<sub>2</sub> desorption peaks; Ni/La<sub>2</sub>Ce<sub>2</sub>O<sub>7</sub>(CP 500) and Ni/La<sub>2</sub>Ce<sub>2</sub>O<sub>7</sub>(CP 600) feature a desorption peak located at 100 °C representing weakly basic sites while the desorption peak at 332 °C is associated with the strongly basic sites. Additionally, the desorption peak of Ni/La<sub>2</sub>Ce<sub>2</sub>O<sub>7</sub>(CP 600) representing the strongly basic sites shows an obviously larger area, demonstrating that the number of strongly basic sites on this catalyst is higher, which is beneficial for CO<sub>2</sub> adsorption. For the Ni/La<sub>2</sub>Ce<sub>2</sub>O<sub>7</sub>(CP 700) catalyst, the desorption peaks, ascribed to moderately strong basic sites, shifts to a low temperature (277 °C), and the degree of overlap between the two desorption peaks is reinforced. This indicates a slight weakening of the basicity of Ni/La<sub>2</sub>Ce<sub>2</sub>O<sub>7</sub>(CP 700), which is unfavorable for CO<sub>2</sub> adsorption.

To further investigate the content and nature of oxygen species on the catalyst surface, XPS measurement was performed. The O1s spectra of the reduced catalysts are shown in Figure 10, and the quantities of surface oxygen species are accordingly tabulated in Table 4. According to the literature [14], XPS spectra of O1s located at low binding energies correspond to lattice oxygen species, while those at high binding energies are related to adsorbed oxygen species. As observed, the Ni/La<sub>2</sub>Ce<sub>2</sub>O<sub>7</sub>(CP 600) catalyst has the highest content of oxygen vacancies on the surface, followed by Ni/La<sub>2</sub>Ce<sub>2</sub>O<sub>7</sub>(CP 500), with Ni/La<sub>2</sub>Ce<sub>2</sub>O<sub>7</sub>(CP 700) showing the least amount. XRD results (Figure 8) indicated that pre-reduction made the crystal size of the support with different calcination temperatures converge to the same. Based on the XPS results, it appears that this pre-treatment also affected the re-distribution of oxygen species on the catalyst surface.



**Figure 10.** XPS profiles of reduced Ni/La<sub>2</sub>Ce<sub>2</sub>O<sub>7</sub> catalysts (O1s, violet: O<sub>2</sub><sup>−</sup>. Blue: CO<sub>3</sub><sup>2−</sup>, olive: O<sub>2</sub><sup>2−</sup>, magenta: O<sup>2−</sup>).

**Table 4.** Quantities of surface oxygen species based on XPS.

Catalyst	O 1s B.E (eV)/Relative Amount (%)				(O <sub>2</sub> <sup>−</sup> + O <sub>2</sub> <sup>2−</sup> )/O <sup>2−</sup>
	O <sub>2</sub> <sup>−</sup>	CO <sub>3</sub> <sup>2−</sup>	O <sub>2</sub> <sup>2−</sup>	O <sup>2−</sup>	
Ni/La <sub>2</sub> Ce <sub>2</sub> O <sub>7</sub> (CP 500)	533.0/7.80	531.4/40.16	530.0/13.39	528.7/38.64	0.54
Ni/La <sub>2</sub> Ce <sub>2</sub> O <sub>7</sub> (CP 600)	533.0/8.63	531.3/43.50	529.6/12.16	528.6/35.7	0.58
Ni/La <sub>2</sub> Ce <sub>2</sub> O <sub>7</sub> (CP 700)	533.1/2.89	531.3/52.43	529.4/7.55	528.6/37.12	0.28

The relative content of adsorbed oxygen species plays a significant role in both the cleavage of CH<sub>4</sub> and the activation of CO<sub>2</sub>. Generally, the cleavage of CH<sub>4</sub> is mainly influenced by the size and activity of the Ni particles and the interaction of the supports [38–40]; however, when the difference between these two factors is not substantial, the cleavage of CH<sub>4</sub> is then correlated to the adsorbed oxygen species, which is able to promote the cleavage of CH<sub>4</sub> [14]. From Table 4, the Ni/La<sub>2</sub>Ce<sub>2</sub>O<sub>7</sub>(CP 600) catalyst after reduction exhibits the largest peak area corresponding to adsorbed oxygen species, i.e., the highest relative content of adsorbed oxygen species, while the relative content of lattice oxygen shows the following trend in the relative content of adsorbed oxygen species on the surface of the three catalysts: Ni/La<sub>2</sub>Ce<sub>2</sub>O<sub>7</sub>(CP 600) > Ni/La<sub>2</sub>Ce<sub>2</sub>O<sub>7</sub>(CP 500) > Ni/La<sub>2</sub>Ce<sub>2</sub>O<sub>7</sub>(CP 700). The above results indicate that the Ni/La<sub>2</sub>Ce<sub>2</sub>O<sub>7</sub>(CP 600) catalyst is able to better catalyze CH<sub>4</sub> and CO<sub>2</sub> when the effect of Ni is factored out.

The reduced Ni/La<sub>2</sub>Ce<sub>2</sub>O<sub>7</sub>(CP T) catalysts were further characterized by TEM, and the results are shown in Figure 11. It is seen that there is no significant difference in the morphology of the different supports, which is consistent with XRD results (Figure 8c). In addition, Ni particles are clearly observed on the surface of all samples (as shown by the yellow circles in Figure 11). From the statistical average Ni particle size, the average Ni particle size is in the following order: Ni/La<sub>2</sub>Ce<sub>2</sub>O<sub>7</sub>(CP 700) > Ni/La<sub>2</sub>Ce<sub>2</sub>O<sub>7</sub>(CP 500) > Ni/La<sub>2</sub>Ce<sub>2</sub>O<sub>7</sub>(CP 600), and the Ni particle size distribution on the Ni/La<sub>2</sub>Ce<sub>2</sub>O<sub>7</sub>(CP 600) is more concentrated. This indicates that the active component, Ni, is more effectively dispersed on the La<sub>2</sub>Ce<sub>2</sub>O<sub>7</sub>(CP 600) support. For the Ni/La<sub>2</sub>Ce<sub>2</sub>O<sub>7</sub>(CP 700) catalyst, the average particle size of the active component, Ni, is the largest and the particle distribution is the widest, indicating that the La<sub>2</sub>Ce<sub>2</sub>O<sub>7</sub>(CP 700) support is less favorable for dispersing the active component due to its larger crystal size compared to the other two.

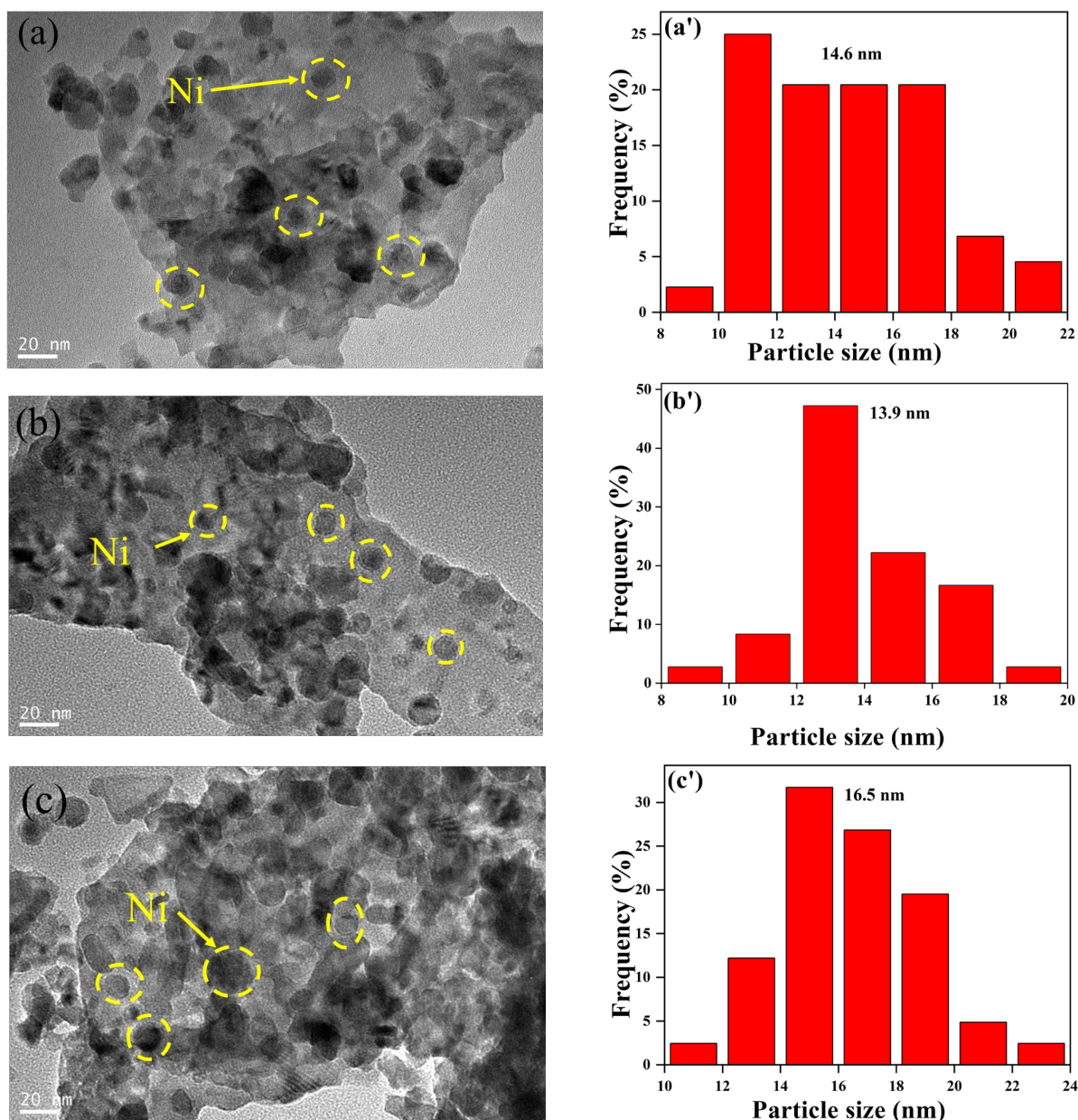


**Figure 11.** TEM images of reduced (a) Ni/La<sub>2</sub>Ce<sub>2</sub>O<sub>7</sub>(CP 500), (b) Ni/La<sub>2</sub>Ce<sub>2</sub>O<sub>7</sub>(CP 600), and (c) Ni/La<sub>2</sub>Ce<sub>2</sub>O<sub>7</sub>(CP 700); particle size distribution of reduced (a') Ni/La<sub>2</sub>Ce<sub>2</sub>O<sub>7</sub>(CP 500), (b') Ni/La<sub>2</sub>Ce<sub>2</sub>O<sub>7</sub>(CP 600), and (c') Ni/La<sub>2</sub>Ce<sub>2</sub>O<sub>7</sub>(CP 700).

From the above, it can be recognized that the calcination temperature of the support also affects the particle size of La<sub>2</sub>Ce<sub>2</sub>O<sub>7</sub> support prepared using the co-precipitation method, with the order of Ni/La<sub>2</sub>Ce<sub>2</sub>O<sub>7</sub>(CP 700) > Ni/La<sub>2</sub>Ce<sub>2</sub>O<sub>7</sub>(CP 500) > Ni/La<sub>2</sub>Ce<sub>2</sub>O<sub>7</sub>(CP 600). Moreover, the BET surface area of the support decreases with the increase in particle size. However, an appropriate particle size leads to stronger metal–support interactions and more surface O vacancies.

#### 2.2.2. The Performance of Ni/La<sub>2</sub>Ce<sub>2</sub>O<sub>7</sub>(CP T)

The as-prepared Ni/La<sub>2</sub>Ce<sub>2</sub>O<sub>7</sub>(CP T) catalysts for DRM performance were tested at 700 °C with a ratio of CH<sub>4</sub>/CO<sub>2</sub> = 1, and the results are shown in Figure 12. It can be seen that the DRM performance of the catalysts has a large difference. The Ni/La<sub>2</sub>Ce<sub>2</sub>O<sub>7</sub>(CP 600) catalyst demonstrates the best activity, while the Ni/La<sub>2</sub>Ce<sub>2</sub>O<sub>7</sub>(CP 700) catalyst exhibits the worst activity. Based on the previous analysis, it seems that the differences in

physical properties such as the particle size and specific surface area of the three catalysts are not significant. Therefore, the contrasting performance is mainly attributed to the differences in chemical properties of the catalyst surfaces. H<sub>2</sub>-TPR, XPS and TEM analyses (Figure 9a, Table 4 and Figure 11) revealed that the interaction between the active component, Ni, and the support is more similar in Ni/La<sub>2</sub>Ce<sub>2</sub>O<sub>7</sub>(CP 500) and Ni/La<sub>2</sub>Ce<sub>2</sub>O<sub>7</sub>(CP 600) catalysts. However, La<sub>2</sub>Ce<sub>2</sub>O<sub>7</sub>(CP 600) with more adsorbed oxygen species is more favorable for dispersing the active component, which is beneficial for promoting the cleavage of CH<sub>4</sub>. From the results of CO<sub>2</sub>-TPD and XPS, the Ni/La<sub>2</sub>Ce<sub>2</sub>O<sub>7</sub>(CP 600) catalyst has more strongly basic sites and more surface oxygen vacancies, which are more advantageous for the adsorption and activation of CO<sub>2</sub>. Rightly, the Ni/La<sub>2</sub>Ce<sub>2</sub>O<sub>7</sub>(CP 600) catalyst has superior DRM reaction performance. For the Ni/La<sub>2</sub>Ce<sub>2</sub>O<sub>7</sub>(CP 700) catalyst, the interaction between the active component and the support is weak, resulting in poor dispersion of the active component on the La<sub>2</sub>Ce<sub>2</sub>O<sub>7</sub>(CP 700), which is unfavorable to the CH<sub>4</sub> cracking; moreover, the surface basicity of this catalyst is weak and the relative content of oxygen vacancies is low, which is not favorable for the adsorption and activation of CO<sub>2</sub>; thus, the DRM reaction performance of Ni/La<sub>2</sub>Ce<sub>2</sub>O<sub>7</sub>(CP 700) catalyst is notably poor. Combined with XRD and N<sub>2</sub> sorption at low temperatures (Figure 8 and Table 3), it is concluded that the optimal particle size of the pyrochlore support is beneficial for both enhancing Ni dispersion and maintaining a balance between carbon deposition and the removal rate in DRM.

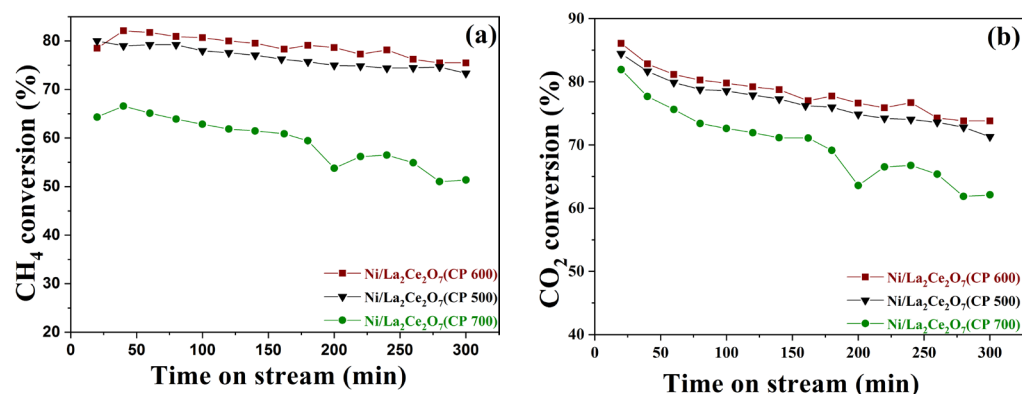


**Figure 12.** Dependence of catalytic performance of reduced Ni/La<sub>2</sub>Ce<sub>2</sub>O<sub>7</sub>(CP T) catalysts on reaction time. (a) CH<sub>4</sub> conversion; (b) CO<sub>2</sub> conversion. Reaction condition: T = 700 °C, CH<sub>4</sub>/CO<sub>2</sub> = 1, GHSV = 48,000 mL/(g·h).

### 2.2.3. Characterization of the Spent Ni/La<sub>2</sub>Ce<sub>2</sub>O<sub>7</sub>(CP T)

Figure 13 gives the characterization results of the spent Ni/La<sub>2</sub>Ce<sub>2</sub>O<sub>7</sub>(CP T) catalysts. As the XRD patterns in Figure 13a outline, the crystalline structure of the support does not change significantly during the reaction, indicating that the catalysts have good thermal stability. The DTA curves of the spent catalysts (Figure 13b) notably suggest that the Ni/La<sub>2</sub>Ce<sub>2</sub>O<sub>7</sub>(CP 700) with the poorest performance has the largest percentage of carbon weight loss. Moreover, the weight loss ratios of the three catalysts are in the opposite order of their activities. The Ni/La<sub>2</sub>Ce<sub>2</sub>O<sub>7</sub>(CP 600) catalyst presents minimal carbon accumulation, probably ascribed to its relatively high Ni dispersion and more oxygen species on the surface. From the DTA curves (Figure S2), the three catalysts show exothermic peaks at approximately 475 °C, demonstrating that the same type of carbon accumulation exists on the three catalysts, which is assigned to C<sub>β</sub>. The spent Ni/La<sub>2</sub>Ce<sub>2</sub>O<sub>7</sub>(CP 600) shows a slightly lower temperature exothermic peak (Figure S2), indicating that the carbon deposited on this catalyst is more reactive compared to the other two catalysts.

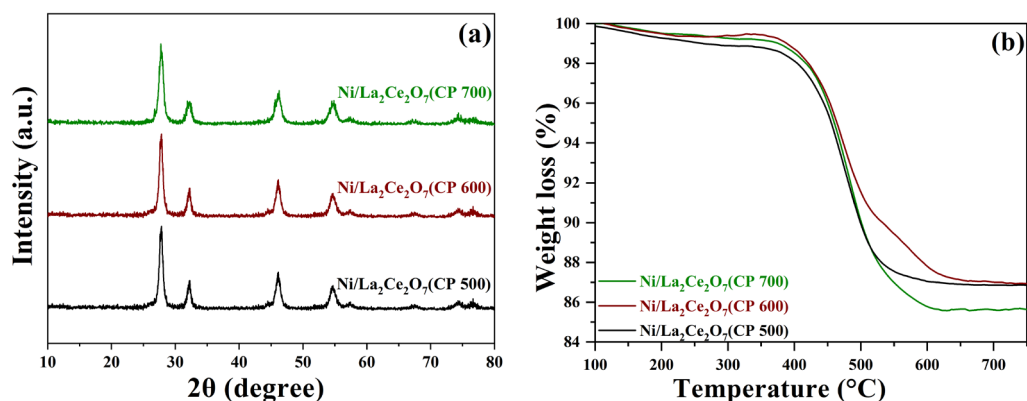


Figure 13. XRD (a) and TG profiles (b) of spent Ni/La<sub>2</sub>Ce<sub>2</sub>O<sub>7</sub>(CP T) catalysts.

### 3. Materials and Methods

#### 3.1. Catalyst Preparation

##### 3.1.1. La<sub>2</sub>Ce<sub>2</sub>O<sub>7</sub> Supports Preparation

La<sub>2</sub>Ce<sub>2</sub>O<sub>7</sub> supports were prepared by using glycine nitrate combustion (GNC), sol-gel (S-G) methods and co-precipitation (CP), respectively, and accordingly defined as La<sub>2</sub>Ce<sub>2</sub>O<sub>7</sub>(GNC), La<sub>2</sub>Ce<sub>2</sub>O<sub>7</sub>(S-G), and La<sub>2</sub>Ce<sub>2</sub>O<sub>7</sub>(CP).

For the preparation of La<sub>2</sub>Ce<sub>2</sub>O<sub>7</sub>(GNC), it is described as follows. Simply, the phased Ce(NO<sub>3</sub>)<sub>3</sub>·6H<sub>2</sub>O and La(NO<sub>3</sub>)<sub>3</sub>·6H<sub>2</sub>O with a molar ratio of 1:1 were dissolved into deionized water to obtain 0.1 mol/L of Ce<sup>3+</sup> + La<sup>3+</sup> aqueous solution. Then, the glycine was added into the above solution at a 1:2 ratio of Ce/glycine, continuously stirring for 30 min until complete dissolution. The resulting solution was slowly placed in the water bath and heated to 80 °C for slow evaporation until forming sticky gel. After that, the gel was transferred to an oven heated to 220 °C for the occurrence of combustion. Subsequently, the obtained fluffy powder was further calcined at 500 °C for 4 h, obtaining the La<sub>2</sub>Ce<sub>2</sub>O<sub>7</sub>(GNC) support.

La<sub>2</sub>Ce<sub>2</sub>O<sub>7</sub>(S-G) support was obtained through the following operation. First, Ce(NO<sub>3</sub>)<sub>3</sub>·6H<sub>2</sub>O and La(NO<sub>3</sub>)<sub>3</sub>·6H<sub>2</sub>O with a molar ratio of 1:1 were dissolved into deionized water to obtain 0.1 mol/L of Ce<sup>3+</sup> + La<sup>3+</sup> aqueous solution, continuously stirring for 30 min; then, the citric acid with 1.2 times the La amount was added into the above solution under stirring. After that, the pH of the solution was adjusted by slowly dropping 37% ammonia aqueous solution to 2. Following, the resulting solution was dried at 80 °C until forming sticky gel. After being further dried for 12 h at 130 °C, the gel was calcined at 500 °C for 4 h, thereafter obtaining the La<sub>2</sub>Ce<sub>2</sub>O<sub>7</sub>(S-G) support.

The La<sub>2</sub>Ce<sub>2</sub>O<sub>7</sub>(CP) support was prepared as described in the following process. Typically, Ce(NO<sub>3</sub>)<sub>3</sub>·6H<sub>2</sub>O and La(NO<sub>3</sub>)<sub>3</sub>·6H<sub>2</sub>O aqueous solution was obtained as the above operation. Then, the Ce<sup>3+</sup> and La<sup>3+</sup> ions were precipitated by adding 37% ammonia aqueous solution dropwise until a pH of 10 along with vigorous stirring. After additional stirring for 30 min, the suspension was filtered and washed several times with deionized water. Subsequently, the resulting cake was dried at 110 °C for 12 h and further calcined at 500 °C for 4 h. Based on different calcination temperatures, the above three supports were defined as La<sub>2</sub>Ce<sub>2</sub>O<sub>7</sub>(CP 500), La<sub>2</sub>Ce<sub>2</sub>O<sub>7</sub>(CP 600) and La<sub>2</sub>Ce<sub>2</sub>O<sub>7</sub>(CP 700).

##### 3.1.2. Preparation of Ni/La<sub>2</sub>Ce<sub>2</sub>O<sub>7</sub> Catalysts

The present catalysts were all prepared using a wet-impregnation method. Simply, well-weighted Ni(NO<sub>3</sub>)<sub>2</sub>·6H<sub>2</sub>O was dissolved into 30 mL alcohol with the ultrasonic assistance to impregnate the above-prepared La<sub>2</sub>Ce<sub>2</sub>O<sub>7</sub> support fine powder. The resulting suspension was stirred at room temperature for 2 h, and the slurry was dried under vacuum (in a rotary evaporator) and further dried at 110 °C overnight. The collected powder was calcined at 500 °C for 4 h. The obtained catalysts were denoted as Ni/La<sub>2</sub>Ce<sub>2</sub>O<sub>7</sub>. Incidentally, the Ni loading of the catalysts was 5wt% unless otherwise specified.

### 3.2. Catalyst Characterization

X-ray diffraction (XRD) patterns of as-prepared samples were recorded using an X-ray diffractometer (Rigaku MiniFlex, Tokyo, Japan) with Cu K $\alpha$  radiation (40 kV, 15 mA). The Debye–Scherrer equation was used to calculate the crystalline size of the particles.

The textural parameters of the catalysts were obtained on Micromeritics ASAP 2020 (Norcross, GA, USA) through N<sub>2</sub> sorption at a low temperature (−196 °C). The specific surface area and pore size distribution were calculated, respectively, based on the BET model and the Brunauer–Emmet–Teller (BJH) model using the desorption branch.

Transmission electron microscope (TEM) images of the samples were viewed on JEOL JEM-2100 (Tokyo, Japan) at 200 kV. The sample was first dispersed in ethanol using ultrasound irradiation. Then, the resulting suspension was dropped onto a carbon-coated copper grid (200 mesh) and air dried.

X-ray photoelectron spectroscopy (XPS) measurement was performed on an Shimadzu Axis Ultra Dld instrument (Kyoto, Japan) with Al K $\alpha$  radiation. The binding energy (BE) was calibrated against the C1s signal (284.8 eV) of contaminant carbon.

The reducibility of the catalysts was characterized using the H<sub>2</sub>-temperature-programmed reduction (H<sub>2</sub>-TPR) technique on a Xianquan chemisorption instrument (TP-5080) (Tianjin, China). A measure of 100 mg of catalyst was pretreated at 300 °C under a flow of Ar (30 mL/min) for 1 h to remove possible humidity and impurities and then cooled to 50 °C. Subsequently, the flow gas was switched to a 10 vol% H<sub>2</sub>/N<sub>2</sub> flow (30 mL/min). After a flat baseline, the temperature-programmed reduction was carried out from 50 °C to 700 °C with a ramp of 10 °C/min.

CO<sub>2</sub> temperature programmed desorption (CO<sub>2</sub>-TPD) was examined on a Xianquan chemisorption instrument (TP-5080) (Tianjin, China). Briefly, the sample after removing humidity was pre-reduced at 700 °C for 60 min at 10vol% H<sub>2</sub>/Ar flow then cooled to 50 °C with an Ar atmosphere. After that, the sample was exposed in CO<sub>2</sub> flow (30 mL/min) for 30 min. Then, pure Ar (30 mL/min) was introduced until the baseline of the TCD was stable. Finally, CO<sub>2</sub> desorption was carried out at a heating rate of 10 °C/min within a range of 50–700 °C, wherein the CO<sub>2</sub> desorption signals were monitored using the TCD detector.

Thermogravimetric analysis (TG) and differential thermal analysis (DTA) was used to monitor the weight loss of the spent catalysts with the temperature rising, carried out using a Rigaku TG-DTA 8120 thermogravimetric analyzer (Tokyo, Japan). The sample (10 mg) was heated from room temperature to 850 °C at a rate of 10 °C/min under an air atmosphere.

### 3.3. Catalyst Test

DRM reaction was performed on a quartz fixed-bed microreactor ( $\Phi$  8 mm) system, in which a cannula was equipped along the axis to fix thermocouple. The catalyst of 200 mg (20~40 meshes) was diluted with quartz sand (20~40 meshes) of 1000 mg. Before each test, the catalyst was pre-reduced at 700 °C for 60 min under 10% H<sub>2</sub>/Ar (*v/v*, 30 mL/min). Subsequently, it was switched to the mixed gas of CH<sub>4</sub> and CO<sub>2</sub> (*v/v* = 1/1) with GHSV = 48,000 mL/(g·h) to start the reaction. The effluent gases at the outlet were analyzed online using a gas chromatograph.

The conversions of CH<sub>4</sub> and CO<sub>2</sub> and H<sub>2</sub>/CO ratio were calculated using Equations (2)–(4):

$$\text{CH}_4 \text{ conversion}(\%) = \frac{V_{\text{CH}_4, \text{in}} - V_{\text{CH}_4, \text{out}}}{V_{\text{CH}_4, \text{in}}} \times 100\% \quad (3)$$

$$\text{CO}_2 \text{ conversion}(\%) = \frac{V_{\text{CO}_2, \text{in}} - V_{\text{CO}_2, \text{out}}}{V_{\text{CO}_2, \text{in}}} \times 100\% \quad (4)$$

$$\text{H}_2/\text{CO ratio} = \frac{V_{\text{H}_2, \text{out}}}{V_{\text{CO}, \text{out}}} \quad (5)$$

where  $V_{i, \text{in}}$  is the volume rate of each fed gas at the inlet,  $V_{i, \text{out}}$  is the volume rate of each effluent gas at the outlet, and *i* represents the gas component.

#### 4. Conclusions

Pyrochlore-type  $\text{La}_2\text{Ce}_2\text{O}_7$  supports were prepared using glycine nitrate combustion (GNC), sol–gel (S-G) methods and co-precipitation (CP), respectively, and a series of  $\text{La}_2\text{Ce}_2\text{O}_7$ (CP) supports were prepared at different calcination temperatures. These supports were used to disperse the Ni component so as to fabricate the catalysts for DRM. The following important results were obtained:

- (1) Compared with the catalysts prepared using sol–gel and combustion methods, the precipitated  $\text{La}_2\text{Ce}_2\text{O}_7$ (CP 500) catalysts (Ni/ $\text{La}_2\text{Ce}_2\text{O}_7$ (CP 500)) show the best DRM reactivity and good stability after Ni loading.
- (2) The supports prepared through different methods have different particle sizes and surface properties. Moreover, improving the calcination temperature can promote the aggregation of the support with a small particle size (below 95 nm) but has no influence on the support with a large particle size (such as  $\text{La}_2\text{Ce}_2\text{O}_7$ -SG with 229 nm). Pre-reduction at 700 °C also leads to the aggregation of  $\text{La}_2\text{Ce}_2\text{O}_7$  support particles calcined below 700 °C.
- (3) An appropriate particle size (68 nm) of the support is beneficial for enhancement of the metal–support interaction and improvement of Ni dispersion, effectively promoting the cracking of  $\text{CH}_4$ . Meanwhile, supports with an appropriate particle size have more oxygen vacancies, leading to the presence of more surface-adsorbed oxygen species and basic sites for  $\text{CO}_2$  adsorption, accelerating carbon removal on the catalyst surface. Thus, the catalyst obtained with  $\text{La}_2\text{Ce}_2\text{O}_7$ (CP 600), which has the most appropriate size, shows optimal catalytic performance in DRM among the representative catalysts.

**Supplementary Materials:** The following supporting information can be downloaded at: <https://www.mdpi.com/article/10.3390/molecules29081871/s1>, Figure S1:  $\text{N}_2$  isotherms and pore distribution of the prepared supports and Ni-loaded catalysts. Figure S2: DTA profiles of spent Ni/ $\text{La}_2\text{Ce}_2\text{O}_7$ (CP T) catalysts.

**Author Contributions:** Y.H.: Supervision and Writing—Review and Editing; J.Z.: Supervision, Writing—Original Draft and Writing—Review and Editing; Q.Z.: Funding Acquisition and Writing—Review and Editing; Z.Z.: Methodology, Formal Analysis and Writing—Original Draft; C.L.: Formal Analysis and Writing—Original Draft; Q.G.: Formal Analysis; J.W.: Formal Analysis. All authors have read and agreed to the published version of the manuscript.

**Funding:** This study was supported by the National Natural Science Foundation of China (No. 22172187) and the Central Guidance on Local Science and Technology Development Fund of Shanxi Province (No. YDZJSX2022A073).

**Institutional Review Board Statement:** Not applicable.

**Informed Consent Statement:** Not applicable.

**Data Availability Statement:** The original contributions presented in the study are included in the article and Supplementary Materials, further inquiries can be directed to the corresponding author.

**Conflicts of Interest:** The authors declare no conflicts of interest.

#### References

1. Aziz, M.A.A.; Jalil, A.A.; Wongsakulphasatch, S.; Vo, D.-V.N. Understanding the role of surface basic sites of catalysts in  $\text{CO}_2$  activation in dry reforming of methane: A short review. *Catal. Sci. Technol.* **2020**, *10*, 35–45. [CrossRef]
2. Yentekakis, I.V.; Panagiotopoulou, P.; Artemakis, G. A review of recent efforts to promote dry reforming of methane (DRM) to syngas production via bimetallic catalyst formulations. *Appl. Catal. B-Environ.* **2021**, *296*, 120210. [CrossRef]
3. Yentekakis, I.V.; Goula, G.; Hatzisymeon, M.; Betsi-Argyropoulou, I.; Botzolaki, G.; Kousi, K.; Kondarides, D.I.; Taylor, M.J.; Parlett, C.M.A.; Osatiashtiani, A.; et al. Effect of support oxygen storage capacity on the catalytic performance of Rh nanoparticles for  $\text{CO}_2$  reforming of methane. *Appl. Catal. B-Environ.* **2019**, *243*, 490–501. [CrossRef]
4. Zhang, X.P.; Zhang, Q.D.; Tsubaki, N.; Tan, Y.S.; Han, Y.Z. Carbon dioxide reforming of methane over Ni nanoparticles incorporated into mesoporous amorphous  $\text{ZrO}_2$  matrix. *Fuel* **2015**, *147*, 243–252. [CrossRef]

5. Das, S.; Ashok, J.; Bian, Z.; Dewangan, N.; Wai, M.H.; Du, Y.; Borgna, A.; Hidajat, K.; Kawi, S. Silica-Ceria sandwiched Ni core-shell catalyst for low temperature dry reforming of biogas: Coke resistance and mechanistic insights. *Appl. Catal. B-Environ.* **2018**, *230*, 220–236. [[CrossRef](#)]
6. Liu, D.P.; Lau, R.; Borgna, A.; Yang, Y.H. Carbon dioxide reforming of methane to synthesis gas over Ni-MCM-41 catalysts. *Appl. Catal. A-Gen.* **2009**, *358*, 110–118. [[CrossRef](#)]
7. Xu, L.L.; Song, H.L.; Chou, L.J. Carbon dioxide reforming of methane over ordered mesoporous NiO-MgO-Al<sub>2</sub>O<sub>3</sub> composite oxides. *Appl. Catal. B-Environ.* **2011**, *108*, 177–190. [[CrossRef](#)]
8. Ma, Q.; Han, Y.; Wei, Q.; Makpal, S.; Gao, X.; Zhang, J.; Zhao, T.-S. Stabilizing Ni on bimodal mesoporous-macroporous alumina with enhanced coke tolerance in dry reforming of methane to syngas. *J. CO<sub>2</sub> Util.* **2020**, *35*, 288–297. [[CrossRef](#)]
9. Chen, J.; Wang, R.; Zhang, J.; He, F.; Han, S. Effects of preparation methods on properties of Ni/CeO<sub>2</sub>-Al<sub>2</sub>O<sub>3</sub> catalysts for methane reforming with carbon dioxide. *J. Mol. Catal. A Chem.* **2005**, *235*, 302–310. [[CrossRef](#)]
10. García-Diéguez, M.; Pieta, I.S.; Herrera, M.C.; Larrubia, M.A.; Alemany, L.J. Nanostructured Pt- and Ni-based catalysts for CO<sub>2</sub>-reforming of methane. *J. Catal.* **2010**, *270*, 136–145. [[CrossRef](#)]
11. Sutthiumporn, K.; Maneerung, T.; Kathiraser, Y.; Kawi, S. CO<sub>2</sub> dry-reforming of methane over La<sub>0.8</sub>Sr<sub>0.2</sub>Ni<sub>0.8</sub>M<sub>0.2</sub>O<sub>3</sub> perovskite (M = Bi, Co, Cr, Cu, Fe): Roles of lattice oxygen on C-H activation and carbon suppression. *Int. J. Hydrog. Energy* **2012**, *37*, 11195–11207. [[CrossRef](#)]
12. Zeling, Z.; Meng, Z.; Junfeng, Z.; Faen, S.; Qingde, Z.; Yisheng, T.; Yizhuo, H. Methane reforming with carbon dioxide over the perovskite supported Ni catalysts. *J. Fuel Chem. Technol.* **2020**, *48*, 833–841.
13. Budiman, A.W.; Song, S.-H.; Chang, T.-S.; Shin, C.-H.; Choi, M.-J. Dry Reforming of Methane Over Cobalt Catalysts: A Literature Review of Catalyst Development. *Catal. Surv. Asia* **2012**, *16*, 183–197. [[CrossRef](#)]
14. Zhang, M.; Zhang, J.; Wu, Y.; Pan, J.; Zhang, Q.; Tan, Y.; Han, Y. Insight into the effects of the oxygen species over Ni/ZrO<sub>2</sub> catalyst surface on methane reforming with carbon dioxide. *Appl. Catal. B-Environ.* **2019**, *244*, 427–437. [[CrossRef](#)]
15. Zhang, M.; Zhang, J.; Zhou, Z.; Chen, S.; Zhang, T.; Song, F.; Zhang, Q.; Tsubaki, N.; Tan, Y.; Han, Y. Effects of the surface adsorbed oxygen species tuned by rare-earth metal doping on dry reforming of methane over Ni/ZrO<sub>2</sub> catalyst. *Appl. Catal. B-Environ.* **2020**, *264*, 118522. [[CrossRef](#)]
16. Pakhare, D.; Shaw, C.; Haynes, D.; Shekhawat, D.; Spivey, J. Effect of reaction temperature on activity of Pt- and Ru-substituted lanthanum zirconate pyrochlores (La<sub>2</sub>Zr<sub>2</sub>O<sub>7</sub>) for dry (CO<sub>2</sub>) reforming of methane (DRM). *J. CO<sub>2</sub> Util.* **2013**, *1*, 37–42. [[CrossRef](#)]
17. Pakhare, D.; Schwartz, V.; Abdelsayed, V.; Haynes, D.; Shekhawat, D.; Poston, J.; Spivey, J. Kinetic and mechanistic study of dry (CO<sub>2</sub>) reforming of methane over Rh-substituted La<sub>2</sub>Zr<sub>2</sub>O<sub>7</sub> pyrochlores. *J. Catal.* **2014**, *316*, 78–92. [[CrossRef](#)]
18. Zhang, X.; Fang, X.; Feng, X.; Li, X.; Liu, W.; Xu, X.; Zhang, N.; Gao, Z.; Wang, X.; Zhou, W. Ni/Ln<sub>2</sub>Zr<sub>2</sub>O<sub>7</sub> (Ln = La, Pr, Sm and Y) catalysts for methane steam reforming: The effects of A site replacement. *Catal. Sci. Technol.* **2017**, *7*, 2729–2743. [[CrossRef](#)]
19. Gao, N.; Cheng, M.; Quan, C.; Zheng, Y. Syngas production via combined dry and steam reforming of methane over Ni-Ce/ZSM-5 catalyst. *Fuel* **2020**, *273*, 117702. [[CrossRef](#)]
20. Hassani Rad, S.J.; Haghghi, M.; Alizadeh Eslami, A.; Rahmani, F.; Rahemi, N. Sol-gel vs. impregnation preparation of MgO and CeO<sub>2</sub> doped Ni/Al<sub>2</sub>O<sub>3</sub> nanocatalysts used in dry reforming of methane: Effect of process conditions, synthesis method and support composition. *Int. J. Hydrog. Energy* **2016**, *41*, 5335–5350. [[CrossRef](#)]
21. Song, Y.-Q.; He, D.-H.; Xu, B.-Q. Effects of preparation methods of ZrO<sub>2</sub> support on catalytic performances of Ni/ZrO<sub>2</sub> catalysts in methane partial oxidation to syngas. *Appl. Catal. A-Gen.* **2008**, *337*, 19–28. [[CrossRef](#)]
22. Wu, J.; Qiao, L.-Y.; Zhou, Z.-F.; Cui, G.-J.; Zong, S.-S.; Xu, D.-J.; Ye, R.-P.; Chen, R.-P.; Si, R.; Yao, Y.-G. Revealing the Synergistic Effects of Rh and Substituted La<sub>2</sub>B<sub>2</sub>O<sub>7</sub> (B = Zr or Ti) for Preserving the Reactivity of Catalyst in Dry Reforming of Methane. *ACS Catal.* **2018**, *9*, 932–945. [[CrossRef](#)]
23. Fang, G.; Wei, C.; Junqiang, X.; Lin, Z. Glow discharge plasma-assisted preparation of nickel-based catalyst for carbon dioxide reforming of methane. *Chin. J. Chem. Phys.* **2008**, *21*, 481–486.
24. Huang, P.; Zhao, Y.; Zhang, J.; Zhu, Y.; Sun, Y. Exploiting shape effects of La<sub>2</sub>O<sub>3</sub> nanocatalysts for oxidative coupling of methane reaction. *Nanoscale* **2013**, *5*, 10844–10848. [[CrossRef](#)] [[PubMed](#)]
25. Zhang, X.; Pei, C.; Chang, X.; Chen, S.; Liu, R.; Zhao, Z.-J.; Mu, R.; Gong, J. FeO<sub>6</sub> Octahedral Distortion Activates Lattice Oxygen in Perovskite Ferrite for Methane Partial Oxidation Coupled with CO<sub>2</sub> Splitting. *J. Am. Chem. Soc.* **2020**, *142*, 11540–11549. [[CrossRef](#)]
26. Zhu, Y.; Zhou, W.; Yu, J.; Chen, Y.; Liu, M.; Shao, Z. Enhancing Electrocatalytic Activity of Perovskite Oxides by Tuning Cation Deficiency for Oxygen Reduction and Evolution Reactions. *Chem. Mater.* **2016**, *28*, 1691–1697. [[CrossRef](#)]
27. Merino, N.A.; Barbero, B.P.; Eloy, P.; Cadús, L.E. La<sub>1-x</sub>Ca<sub>x</sub>CoO<sub>3</sub> perovskite-type oxides: Identification of the surface oxygen species by XPS. *Appl. Surf. Sci.* **2006**, *253*, 1489–1493. [[CrossRef](#)]
28. Zhuang, L.; Ge, L.; Yang, Y.; Li, M.; Jia, Y.; Yao, X.; Zhu, Z. Ultrathin Iron-Cobalt Oxide Nanosheets with Abundant Oxygen Vacancies for the Oxygen Evolution Reaction. *Adv. Mater.* **2017**, *29*, 1606793. [[CrossRef](#)]
29. Wang, N.; Shen, K.; Huang, L.; Yu, X.; Qian, W.; Chu, W. Facile Route for Synthesizing Ordered Mesoporous Ni-Ce-Al Oxide Materials and Their Catalytic Performance for Methane Dry Reforming to Hydrogen and Syngas. *ACS Catal.* **2013**, *3*, 1638–1651. [[CrossRef](#)]
30. Löfberg, A.; Guerrero-Caballero, J.; Kane, T.; Rubbens, A.; Jalowiecki-Duhamel, L. Ni/CeO<sub>2</sub> based catalysts as oxygen vectors for the chemical looping dry reforming of methane for syngas production. *Appl. Catal. B-Environ.* **2017**, *212*, 159–174. [[CrossRef](#)]

31. Hu, Z.; Liu, X.; Meng, D.; Guo, Y.; Guo, Y.; Lu, G. Effect of Ceria Crystal Plane on the Physicochemical and Catalytic Properties of Pd/Ceria for CO and Propane Oxidation. *ACS Catal.* **2016**, *6*, 2265–2279. [[CrossRef](#)]
32. Ferreira, V.J.; Tavares, P.; Figueiredo, J.L.; Faria, J.L. Ce-Doped La<sub>2</sub>O<sub>3</sub> based catalyst for the oxidative coupling of methane. *Catal. Commun.* **2013**, *42*, 50–53. [[CrossRef](#)]
33. Aw, M.S.; Crnivec, I.G.O.; Pintar, A. Tunable ceria-zirconia support for nickel-cobalt catalyst in the enhancement of methane dry reforming with carbon dioxide. *Catal. Commun.* **2014**, *52*, 10–15. [[CrossRef](#)]
34. Zuo, Z.J.; Shen, C.F.; Tan, P.J.; Huang, W. Ni based on dual-support Mg-Al mixed oxides and SBA-15 catalysts for dry reforming of methane. *Catal. Commun.* **2013**, *41*, 132–135. [[CrossRef](#)]
35. Guo, J.; Lou, H.; Zheng, X.M. The deposition of coke from methane on a Ni/MgAl<sub>2</sub>O<sub>4</sub> catalyst. *Carbon* **2007**, *45*, 1314–1321. [[CrossRef](#)]
36. Guzzi, L.; Stefler, G.; Geszti, O.; Sajo, I.; Paszti, Z.; Tompos, A.; Schay, Z. Methane dry reforming with CO<sub>2</sub>: A study on surface carbon species. *Appl. Catal. A-Gen.* **2010**, *375*, 236–246. [[CrossRef](#)]
37. Bychkov, V.Y.; Tyulenin, Y.P.; Firsova, A.A.; Shafranovsky, E.A.; Gorenberg, A.Y.; Korchak, V.N. Carbonization of nickel catalysts and its effect on methane dry reforming. *Appl. Catal. A-Gen.* **2013**, *453*, 71–79. [[CrossRef](#)]
38. Han, J.W.; Park, J.S.; Choi, M.S.; Lee, H. Uncoupling the size and support effects of Ni catalysts for dry reforming of methane. *Appl. Catal. B-Environ.* **2017**, *203*, 625–632. [[CrossRef](#)]
39. Danghyan, V.; Novoa, S.C.; Mukasyan, A.; Wolf, E.E. Pressure dilution, a new method to prepare a stable Ni/fumed silica catalyst for the dry reforming of methane. *Appl. Catal. B-Environ.* **2018**, *234*, 178–186. [[CrossRef](#)]
40. Damyanova, S.; Pawelec, B.; Palcheva, R.; Karakirova, Y.; Sanchez, M.C.C.; Tyuliev, G.; Gaigneaux, E.; Fierro, J.L.G. Structure and surface properties of ceria-modified Ni-based catalysts for hydrogen production. *Appl. Catal. B-Environ.* **2018**, *225*, 340–353. [[CrossRef](#)]

**Disclaimer/Publisher’s Note:** The statements, opinions and data contained in all publications are solely those of the individual author(s) and contributor(s) and not of MDPI and/or the editor(s). MDPI and/or the editor(s) disclaim responsibility for any injury to people or property resulting from any ideas, methods, instructions or products referred to in the content.